

# $\Delta$ -PINNs: physics-informed neural networks on complex geometries

Francisco Sahli Costabal<sup>a,b,c,\*</sup>, Simone Pezzuto<sup>d,e</sup>, Paris Perdikaris<sup>f</sup>

<sup>a</sup>*Department of Mechanical and Metallurgical Engineering, School of Engineering, Pontificia Universidad Católica de Chile, Santiago, Chile*  
<sup>b</sup>*Institute for Biological and Medical Engineering, Schools of Engineering, Medicine and Biological Sciences, Pontificia Universidad Católica de Chile, Santiago, Chile*

<sup>c</sup>*Millennium Institute for Intelligent Healthcare Engineering, iHEALTH*

<sup>d</sup>*Laboratory of Mathematics for Biology and Medicine, Department of Mathematics, Università di Trento, Trento, Italy*

<sup>e</sup>*Center for Computational Medicine in Cardiology, Euler Institute, Università della Svizzera italiana, Lugano, Switzerland*

<sup>f</sup>*Department of Mechanical Engineering and Applied Mechanics, University of Pennsylvania, Philadelphia, Pennsylvania, USA*

---

## Abstract

Physics-informed neural networks (PINNs) have demonstrated promise in solving forward and inverse problems involving partial differential equations. Despite recent progress on expanding the class of problems that can be tackled by PINNs, most of existing use-cases involve simple geometric domains. To date, there is no clear way to inform PINNs about the topology of the domain where the problem is being solved. In this work, we propose a novel positional encoding mechanism for PINNs based on the eigenfunctions of the Laplace-Beltrami operator. This technique allows to create an input space for the neural network that represents the geometry of a given object. We approximate the eigenfunctions as well as the operators involved in the partial differential equations with finite elements. We extensively test and compare the proposed methodology against different types of PINNs in complex shapes, such as a coil, a heat sink and the Stanford bunny, with different physics, such as the Eikonal equation and heat transfer. We also study the sensitivity of our method to the number of eigenfunctions used, as well as the discretization used for the eigenfunctions and the underlying operators. Our results show excellent agreement with the ground truth data in cases where traditional PINNs fail to produce a meaningful solution. We envision this new technique will expand the effectiveness of PINNs to more realistic applications. Code available at: <https://github.com/fsahli/Delta-PINNs>

**Keywords:** deep learning; Laplace-Beltrami eigenfunctions; physics-informed neural networks; Eikonal equation; partial differential equations

---

## 1. Motivation

Physics-informed neural networks (PINNs) [40] are an exciting new tool for blending data and known physical laws in the form of differential equations. They have been successfully applied to multiple physical domains such as fluid mechanics [41], solid mechanics [17], heat transfer [6] and biomedical engineering [26, 43], to name a few. They tend to excel when performing inverse problems when either there partial observations of the quantity of interest or the physics are only approximately satisfied. PINNs can be used for forward problems but, in this area, traditional tools, such as the finite element method tend to be faster and more accurate. Since their inception, there have been multiple attempts to improve PINNs, in areas such as training strategies [36, 55] and activation functions [23].

Despite recent progress, many works still consider simple geometric domains to solve either forward or inverse problems, hindering the applicability of PINNs to real world problems, where the objects of study may have complicated shapes and topologies. In this area, there have been multiple attempts to introduce complexity to the input domain of the neural networks. One approach is to describe the boundary of the domain with a signed distance function [48, 3, 32]. In this way, the boundary conditions can be satisfied exactly instead of relying on a penalty term

---

\*Corresponding author

Email addresses: fsc@ing.puc.cl (Francisco Sahli Costabal), simone.pezzuto@usi.ch (Simone Pezzuto), pgp@seas.upenn.edu (Paris Perdikaris)

in the loss function. Another approach is to use domain decomposition to model smaller but simpler domains [22]. Coordinate mappings between a simple domain have also been proposed for convolutional [15] and fully connected networks [28, 42]. Nonetheless, all these works demonstrate examples of 2-dimensional shapes. When using PINNs in 3-dimensional surfaces there have been attempts to ensure that the vector fields that may appear in the partial differential equations remain tangent to the surface by introducing additional terms in the loss function [13, 45]. This approach works well when the surface is relatively simple and smooth, specifically when the Euclidean distance of the embedding 3-D space between two points in the domain is similar to the intrinsic geodesic distance on the manifold. However, in several applications the two distances may sensibly differ, as exemplified in Figure 1.

In this work, we propose to represent the coordinates of the input geometry with a positional encoding based on the eigenfunctions of the Laplace-Beltrami operator of the manifold, or the Laplacian in the case of a bounded open domain in the Euclidean space. In this way, points that are close in the geometry will remain close in the positional encoding space. The usage of the Laplace-Beltrami operator is widespread in shape analysis [56] because it encodes all information about the geometry up to isometry. Therefore, the eigenfunctions of the operator are a compact positional encoding of the geometrical shape information. Therefore, we propose that the input of the neural network will be the value of a finite number of eigenfunctions evaluated at a point in the domain and the output will remain the physical quantity that we are modeling with PINNs. Positional encoding have shown great success in improving the capabilities of neural networks and are used in transformers [52], neural radiance fields [33], and PINNs [54] to name a few. For our positional encoding, the Laplace-Beltrami eigenfunctions can be approximated numerically for any shape with the finite element method. By approximating the eigenfunctions on a mesh we lose the ability to use automatic differentiation with backpropagation to compute the operators of the partial differential equations within existing machine learning libraries. However, combining machine learning libraries with packages that offer finite element automatic differentiation could make the operator computation automatic [35]. We show that common operators such as the gradient and the Laplacian can be efficiently computed with finite elements applied to the output of the neural network. We demonstrate the capabilities of the proposed method by testing different geometries, such as a coil, a heat sink and a bunny and different physics, such as the Eikonal equation and heat transfer.

This paper is organized as follows. In Section 2 we present a brief overview of the original formulation of physics-informed neural networks, then we introduce the eigenfunctions of the Laplace-Beltrami operator and we present our proposed method, henceforth referred as  $\Delta$ -PINN. In Section 3 we test the methodology by solving an inverse problem involving the Eikonal equation on a coil. We then present an example of an inverse problem of a heat sink where only the external temperature is observed. We continue by solving a forward problem involving the Poisson equation in a squared domain to perform a sensitivity study regarding the hyper-parameters of our method. In all these examples we compare against the performance of traditional PINNs and other types of PINNs specialized for these tasks. We also explore the scaling of the proposed method with respect to the mesh size. We finalize this section by developing a network that learns the geodesic distance between any two points on the surface of a bunny. We end this paper in Section 4 with a discussion of the main findings and an outlook of future work.

## 2. Methods

We begin this section with a brief description of physics-informed neural networks.

### 2.1. Physics-informed neural networks

We consider the problem where we have partial observations of an unknown function  $u(\mathbf{x})$ , with an input domain  $\mathbf{x} \in \mathcal{B}$ , where  $\mathcal{B}$  is an open and bounded domain in  $\mathbb{R}^d$ ,  $d = 2, 3$  or a  $d$ -dimensional smooth manifold (typically a surface). We also assume that  $u(\mathbf{x})$  satisfies a partial differential equation of the form  $\mathcal{N}[u; \lambda] = 0$ , where  $\mathcal{N}[\cdot; \lambda]$  is a potentially non-linear operator parametrized by  $\lambda$ . The partial observations  $u_i$  are located in  $\bar{\mathcal{B}}$  at positions  $\mathbf{x}_i$ ,  $i = 1, \dots, N$ , which may therefore fall on the boundary  $\partial\mathcal{B}$ . Boundary conditions such as Neumann boundary conditions  $\nabla u \cdot \mathbf{n} = g_i$ , may also be enforced at boundary points  $\mathbf{x}_i^b$ ,  $i = 1, \dots, B$ . We proceed by approximating the unknown function with a neural network  $u \approx \hat{u} = \text{NN}(\mathbf{x}, \theta)$ , parametrized with trainable parameters  $\theta$ . In order to learn a function that satisfies the observed data, the boundary conditions and the partial differential equation, we postulate a loss function composed of three terms

$$\mathcal{L}(\{u_i, \mathbf{x}_i\}, \{g_i, \mathbf{x}_i^b\}, \theta, \lambda) = \text{MSE}_{\text{data}}(\{u_i, \mathbf{x}_i\}, \theta) + \text{MSE}_{\text{PDE}}(\theta, \lambda) + \text{MSE}_{\text{b}}(\{g_i, \mathbf{x}_i^b\}, \theta). \quad (1)$$

## Laplace-Beltrami eigenfunctions

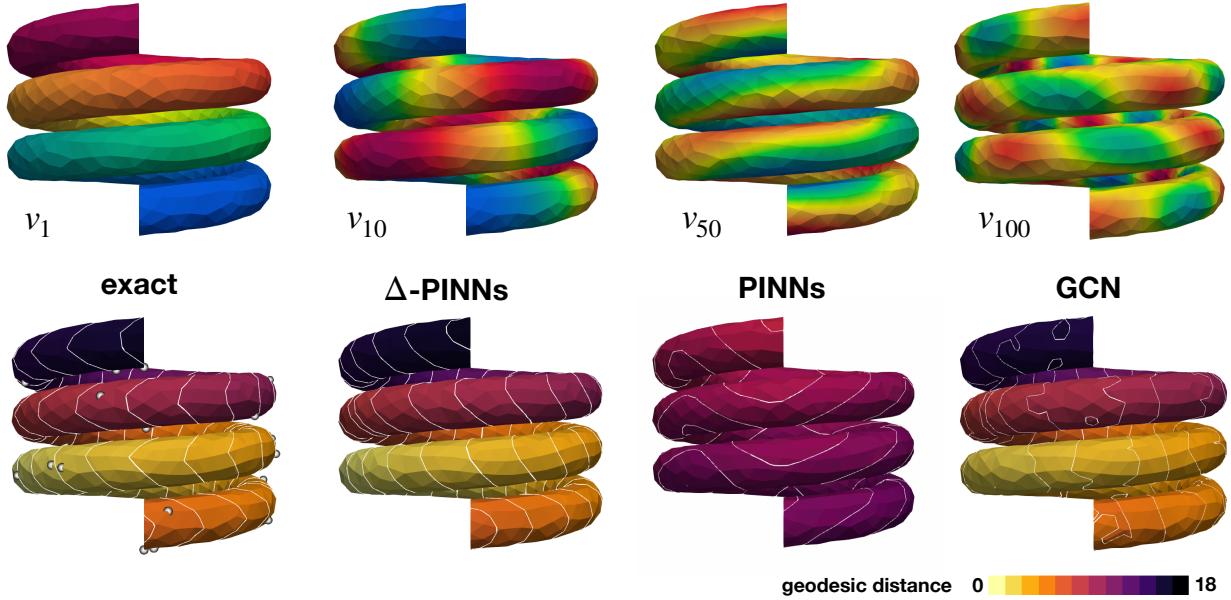


Figure 1: **Learning the Eikonal equation on a coil.** Top row: the 1<sup>st</sup>, 10<sup>th</sup>, 50<sup>th</sup> and 100<sup>th</sup> Laplace-Beltrami eigenfunction of the geometry. Bottom row, first: the ground truth solution of the Eikonal equation, which represents the geodesic distance, and the data points used for training shown as gray spheres. Second, the solution of  $\Delta$ -PINNs, our proposed method trained with 50 eigenfunctions. Third, the traditional PINNs approximation. Last, the approximate solution of a physics-informed graph-convolution network.

The first term favours the network to learn the available data

$$\text{MSE}_{\text{data}}(\{u_i, \mathbf{x}_i\}, \boldsymbol{\theta}) = \frac{1}{N} \sum_i^N (u_i - \hat{u}(\mathbf{x}_i; \boldsymbol{\theta}))^2. \quad (2)$$

The second term ensures that the underlying partial differential equation is approximately satisfied

$$\text{MSE}_{\text{PDE}}(\boldsymbol{\theta}, \lambda) = \frac{1}{R} \sum_i^R (\mathcal{N}[\hat{u}(\mathbf{x}_i^r; \boldsymbol{\theta}); \lambda])^2. \quad (3)$$

Here, we will evaluate the model at locations  $\mathbf{x}_i^r$  that can be generated randomly within the domain at every optimization iteration or can have predefined values. Minimizing this term will ensure that the model is approximately satisfied in the entire domain. We can also define the parameters of the operator  $\mathcal{N}[\cdot, \lambda]$  as trainable variables that will be learned during the optimization procedure. The final term in the loss function ensures that Neumann boundary conditions  $\nabla u \cdot \mathbf{n} = g_i$  are satisfied

$$\text{MSE}_{\text{b}}(\{g_i, \mathbf{x}_i^b\}, \boldsymbol{\theta}) = \frac{1}{B} \sum_i^B (\nabla \hat{u}(\mathbf{x}_i^b; \boldsymbol{\theta}) \cdot \mathbf{n} - g_i)^2. \quad (4)$$

This term penalizes difference the flux through the boundary to the prescribed value  $g_i$ . We note that Dirichlet boundary conditions can be included as data in  $\{u_i, \mathbf{x}_i\}$ . This is the basic structure of physics-informed neural networks that can be accommodated for a large class of problems [40]. One issue of this formulation is that the neural network that represents the solution is parametrized with a vector  $\mathbf{x} \in \mathbb{R}^3$ , which is a Euclidean space. In this way, it is difficult to inform the network about the geometry of the domain or, in the case of a complex domain in  $\mathbb{R}^d$  where the boundaries lie. This is important in the computation of the differential operators. Furthermore, points in the manifold  $\mathcal{B}$  that are close in the Euclidean space are not necessarily close in the intrinsic distance, as illustrated in Figure 1.

## 2.2. Eigenfunctions of Laplace-Beltrami operator

In this work, we propose to encode the manifold of interest  $\mathcal{B}$  with the eigenfunctions of the Laplace-Beltrami operator, or the standard Laplace operator when  $\mathcal{B}$  is a flat domain [11], instead of using the Euclidean coordinates  $\mathbf{x}$ . In its strong form, the Laplace operator  $\Delta[\cdot] = (\nabla \cdot \nabla)[\cdot]$  applied to a sufficiently smooth function is the sum of the second-order derivatives of the function:

$$\Delta u(x_1, x_2, \dots, x_d) = \sum_{i=1}^d \frac{\partial u^2}{\partial x_i^2}.$$

For a curved domain or a manifold, the Laplace-Beltrami operator  $\Delta_S[\cdot] = (\nabla_S \cdot \nabla_S)[\cdot]$  only depends on the metric tensor of  $\mathcal{B}$ , see [9]. Therefore,  $\Delta_S$  is intrinsic, that is its definition does not require the ambient space. The Laplace-Beltrami operator is also invariant to isometric transformations (translation, rotation).

The eigenfunctions  $v_i(\mathbf{x})$  of the Laplace-Beltrami operator as solutions of the following eigenvalue problem

$$-\Delta_S v_i(\mathbf{x}) = \lambda_i v_i(\mathbf{x}), \quad \mathbf{x} \in \mathcal{B},$$

where  $\lambda_i$  is the correspondent eigenvalue of  $v_i(\mathbf{x})$ . In the case of a domain with open boundaries, this problem is usually accompanied with either homogeneous Dirichlet or Neumann boundary conditions. In this work, we will use the latter. The set of eigenvalues provide a spectral signature of the domain, with manifold applications in shape analysis [56]. It is possible to show that the eigenvalues of the Laplace-Beltrami operator, endowed with homogeneous boundary conditions, are real, non-negative, and tending to infinity. When ordered by their magnitude, the first eigenvalue  $\lambda_0$  is always zero, whereas the second one  $\lambda_1$  is strictly positive. The physical interpretation is that small eigenvalues are associated with low frequency functions, represented by the corresponding eigenfunction. The set of eigenfunctions form an orthogonal basis for the Hilbert space  $L^2(\mathcal{B})$ , hence every function in  $L^2(\mathcal{B})$  can be expressed as a linear combination of the eigenfunctions [11].

The spectrum of  $-\Delta_S$  has several noteworthy properties that make it an ideal candidate for positional encoding: for an extensive review in the context of shape analysis we refer to Wang and Solomon [56]. As for the Laplace-Beltrami operator, eigenvalues and eigenfunctions are invariant to isometries. The geodesic distance  $d_S(\mathbf{x}, \mathbf{y})$  between two points on the manifold is related to the heat kernel via the Varadhan's formula, which in turn can be defined through the Laplace-Beltrami operator:

$$d_S(\mathbf{x}, \mathbf{y}) = \lim_{t \rightarrow 0^+} \sqrt{-4t \log k_t(\mathbf{x}, \mathbf{y})}, \quad k_t(\mathbf{x}, \mathbf{y}) = \sum_i e^{-\lambda_i t} v_i(\mathbf{x}) v_i(\mathbf{y}).$$

Actually, the diffusion distance [7] is directly linked to the eigenfunctions:

$$d_t^2(\mathbf{x}, \mathbf{y}) = \sum_i e^{-2\lambda_i t} (v_i(\mathbf{x}) - v_i(\mathbf{y}))^2,$$

which shows that a positional encoding based on the eigenfunctions would preserve the geodesic distance between points on the manifold.

Although these functions may be computed analytically for a few shapes (e.g., the sphere), their numerical approximation is possible for an arbitrary manifold. Here, we represent the domain  $\mathcal{B}$  using a mesh with nodes and elements and solve the eigenvalue problem using finite element shape functions. As such, we can obtain the discrete Laplacian matrix  $\mathbf{A}$  and mass matrix  $\mathbf{M}$  as

$$\mathbf{A}_{ij} = \sum_{e=1}^{n_{\text{el}}} \int_{\mathcal{B}} \nabla N_i \cdot \nabla N_j d\mathcal{B}, \quad \mathbf{M}_{ij} = \sum_{e=1}^{n_{\text{el}}} \int_{\mathcal{B}} N_i N_j d\mathcal{B}, \quad (5)$$

where  $\mathbf{A}$  represents the assembly of the local element matrices, and  $N$  are the finite element shape functions. Then, we solve the eigenvalue problem:  $\mathbf{A}\mathbf{v} = \lambda \mathbf{M}\mathbf{v}$ , see Appendix A for more details.

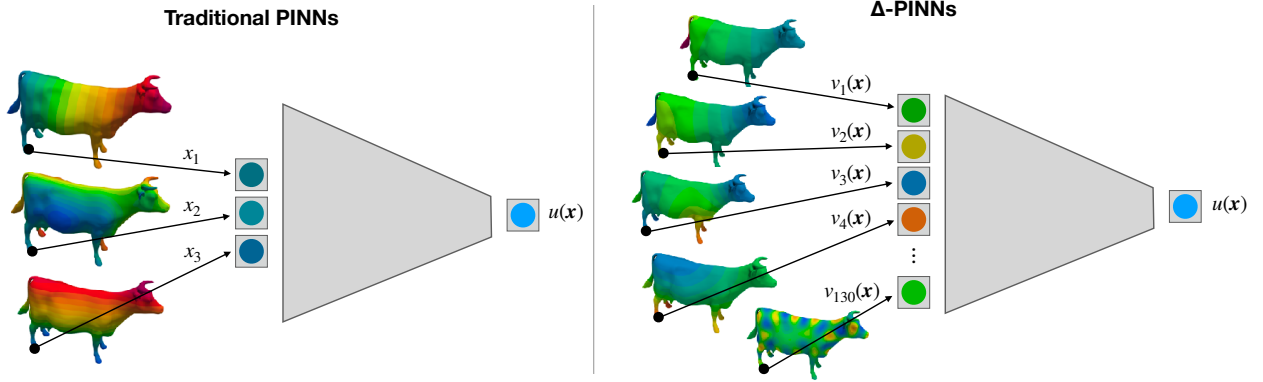


Figure 2: **Traditional PINNs vs.  $\Delta$ -PINNs architecture.** In traditional PINNs, the input layer is the vector of coordinates. With  $\Delta$ -PINN, the input layer is the value of the eigenfunctions at the coordinate of interest. In this way we can encode much more information about the geometry.

### 2.3. Physics-informed neural networks on manifolds

We propose to represent the position of a point in the manifold by  $N$  eigenfunctions of the Laplace-Beltrami operator associated with the  $N$  eigenfunctions associated with the  $N$  lowest eigenvalues, such that  $\mathbf{v}_i = [v_1(\mathbf{x}_i), v_2(\mathbf{x}_i), \dots, v_N(\mathbf{x}_i)]$ . Now, instead of parametrizing the neural network with the Euclidean position, we use:

$$u \approx \hat{u} = \text{NN}(\mathbf{v}(\mathbf{x}), \boldsymbol{\theta}).$$

Since  $\mathbf{v}$  varies smoothly in the manifold, intrinsically close points will be also close in the space  $\mathbf{v}$ , as shown in Figure 2.)

Another interpretation of the proposed method is that we are constructing features or positional encodings for points in the manifold. Then, the approximation of the solution  $\hat{u}$  can be seen as a non-linear combination of these features. In our case, the eigenfunctions represent features of increasing frequency, as seen in Figure 1. A similar concept has been proposed for Cartesian domains with Fourier feature mappings [50, 54]. Here, the Cartesian coordinates are transformed with sine and cosine functions, which have random frequencies that can be tuned for the problem of interest. The main difference is that in our method the frequencies are given by the eigenfunctions, and are defined in the manifold where we want to solve the problem. We can select different eigenfunctions depending on the nature of the problem, where high frequency problems might need a larger amount of eigenfunctions.

The main challenge of our methodology is that the differential operators cannot be computed directly from the neural network via automatic differentiation. Since the eigenfunctions cannot be computed in closed form for an arbitrary manifold, we have a map between  $\mathbf{x}$  and  $\mathbf{v}$  that is defined using finite elements. The only way to differentiate the eigenfunctions  $\mathbf{v}$  with respect to the position  $\mathbf{x}$  is again by using finite elements. Therefore, we use this numerical approximation of the differential operators that are required to compute the PDE operator  $\mathcal{N}[\cdot]$ . Commonly used operators, such as the gradient and the Laplacian can be easily computed with linear finite elements. We also note that one could employ the chain rule to compute, for example, the gradient, such that  $\nabla_{\mathbf{x}} \hat{u} = \nabla_{\mathbf{v}} \hat{u} \cdot \nabla_{\mathbf{x}} \mathbf{v}$ . The term  $\nabla_{\mathbf{v}} \hat{u}$  can be computed with automatic differentiation since it only depends on the neural network, and the second term  $\nabla_{\mathbf{x}} \mathbf{v}$  needs to be computed with finite elements. This is done in Sec. 3.6, for instance. We found small advantages with this approach, and it becomes cumbersome for second order operators.

Alternatively, we use the neural network predictions at the nodal locations and use finite elements to evaluate the operator. In other words, we apply the differential operators to the piecewise-linear interpolant of the neural network. We define the nodal values of the interpolant, denoted by  $\mathcal{I}_h \hat{u}$  as follows:

$$(\mathcal{I}_h \hat{u})_i := \hat{u}(\mathbf{x}_i) = \text{NN}(\mathbf{v}(\mathbf{x}_i), \boldsymbol{\theta}).$$

For neural networks with differentiable activation functions, the interpolant approximates the NN with a  $O(h^2)$ -error in the infinity norm [38]. To approximate the gradient  $\nabla_{\mathbf{x}} \hat{u}$ , a piecewise-constant function on each triangular element of the mesh, we simply use the formula

$$\nabla_{\mathbf{x}} \hat{u}|_e \approx \nabla_{\mathbf{x}} \mathcal{I}_h \hat{u}|_e = \mathbf{B}^e \cdot [\hat{u}_1, \hat{u}_2, \hat{u}_3]^T, \quad (6)$$

where the matrix  $\mathbf{B}^e$  defines the gradient operator for a linear triangular element  $e$ , see Appendix A. One of the advantages of this approach is that the gradient is guaranteed to be tangent to the manifold, which is not the case for the traditional physics-informed neural network formulation [45].

Similarly, we can compute the Laplacian  $\Delta\hat{u}_i$  at any given nodal location by predicting  $\hat{u}_j$  at all the neighboring nodes, including the node of interest. Then, we can use the definition of the discrete Laplacian presented in Eq. (5), namely

$$-\Delta\hat{u}_i \approx \sum_{j,k} \mathbf{M}_{ij}^{-1} \mathbf{A}_{jk} \hat{u}_k = \sum_k \mathbf{L}_{ik} \hat{u}_k, \quad (7)$$

where we introduced the discrete Laplace-Beltrami operator  $\mathbf{L} := \mathbf{M}^{-1} \mathbf{A}$ . The operator  $\mathbf{L}$  is full and thus not worth assembling in general. The advantage of being able to compute the operators locally at the element or node level is that we can still use mini-batch techniques to estimate the loss function and its gradient. In this way, we avoid predicting the operator for the entire manifold, which could slow the training process for large meshes. In general, we will randomly select nodes or elements for each training iteration to evaluate the loss term  $\text{MSE}_{\text{PDE}}$  defined in Eq. (3).

In what follows, we consider 3 options.

1. We formulate the problem in terms of energy, whenever possible. This is the case of the Poisson equation and hyperelasticity problems with conservative boundary conditions, for instance. The energy for these problems involves the gradient, which can be locally approximated with Eq. (6). See Sec. 3.4 for an example.
2. We minimize the residual of the finite element formulation, which typically involves only local operations. This is done in Secs. 3.2-3.3.
3. We lump the mass matrix, so that the operator  $\mathbf{L}$  is again a local operator [56].

### 3. Numerical experiments

#### 3.1. Eikonal equation on a coil

In our first numerical experiment we compute geodesic distances using the Eikonal equation

$$\begin{cases} \sqrt{\nabla_S u \cdot \nabla_S u} = 1, \\ u(\mathbf{x}_b) = 0, \end{cases} \quad (8)$$

where  $\nabla_S u := \nabla - (\mathbf{n} \cdot \nabla u) \mathbf{n}$  is the surface gradient. This equation has multiple applications, for instance, in cardiac electrophysiology [37, 45] and seismology [47], because it can be used to model the arrival times of a traveling wave. In the particular form shown in Eq. (8), the solution  $u(\mathbf{x})$  can be interpreted as the geodesic distance from the point  $\mathbf{x}_b$  to any point  $\mathbf{x}$  on the manifold.

In this example, we will solve this equation on the surface of a coil, which is generated by an helix with 30 mm of diameter and 12 mm per revolution of pitch. This curve is extruded with a circular cross-section with 5 mm of radius. The resulting geometry can be seen in Figure 1, which is discretized with 1,546 points and 3,044 triangles. We can generate a ground truth solution of the Eikonal equation by randomly selecting a point on the mesh for  $\mathbf{x}_b$  and then applying the exact geodesic algorithm [34] as implemented in libigl [21]. We randomly select 40 points of this solution to use as data  $u_i$ . In this case, the partial differential equation loss defined in (3) takes the form

$$\text{MSE}_{\text{PDE}}(\boldsymbol{\theta}) = \frac{1}{R} \sum_i^R \left( \sqrt{(\mathbf{B}_r^e \hat{u}_r^e) \cdot (\mathbf{B}_r^e \hat{u}_r^e)} - 1 \right)^2, \quad (9)$$

where  $\mathbf{B}_r^e \hat{u}_r^e$  is the approximation of the surface gradient for a particular triangle  $r$ , see Appendix A. Here, the vector  $\hat{u}_r^e$  is the prediction of the neural network at the nodes of the triangle  $r$ , which depends on the trainable parameters  $\boldsymbol{\theta}$ . We remark that we do not impose the initial condition in the loss function, thus the problem is ill-posed and must be supplemented with data points. We use 50 eigenfunctions of the Laplace-Beltrami operator as input of the neural network, which is then followed by a single hidden layer with 100 neurons and hyperbolic tangent activations. We train the neural network with the ADAM optimizer [24] for 40,000 iterations with default parameters. We use a batch

example	coil		heat sink	
method	error	training time (s)	error	training time (s)
PINN	0.98	20.2	$1.48 \cdot 10^{-1}$	187.6
$\Delta$ -PINN	$3.68 \cdot 10^{-3}$	$(0.9) + 54.3$	$1.62 \cdot 10^{-4}$	$(0.5) + 265.8$
GCN	$2.95 \cdot 10^{-2}$	574.4	$1.96 \cdot 10^{-4}$	1341.5
SDF-PINN	-	-	$1.45 \cdot 10^{-4}$	355.1

Table 1: Comparison of mean squared error and training times for the different methods and examples considered. For  $\Delta$ -PINNs, the time to compute all the eigenfunctions of the mesh is given between parenthesis.

size of 10 samples to evaluate both the  $MSE_{data}$  and  $MSE_{PDE}$  term. For comparison, we also train the same neural network by removing the physics, that is not considering the partial differential equation loss shown equation (9). Additionally, we train a regular physics-informed neural network, where we use the Cartesian coordinates as the input of the neural network. We implemented the Eikonal equation in the  $MSE_{PDE}$  computing  $\nabla_S u$  through automatic differentiation. This network has 2 hidden layers with 50 and 100 neurons, respectively. We also tested against a physics-informed graph convolutional network [16], detailed in Appendix B.1, with matched number of parameters. We train all methods for the same number of iterations and learning rate.

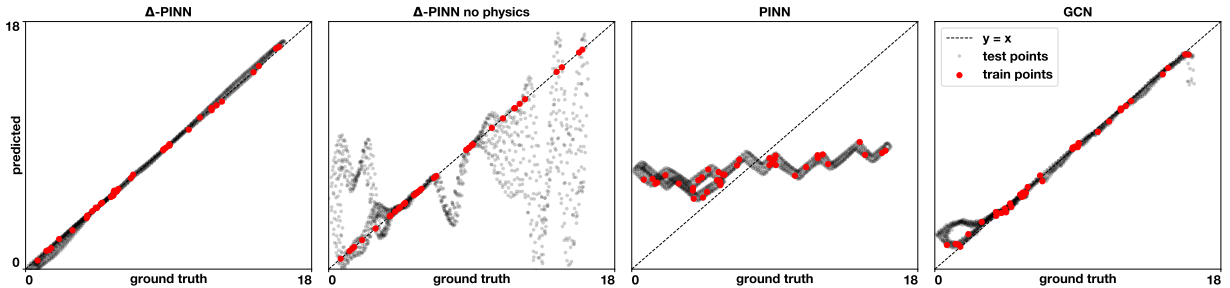


Figure 3: Accuracy of the coil example with the Eikonal equation. Correlation between predicted and ground truth values of geodesic distance for  $\Delta$ -PINNs (first),  $\Delta$ -PINNs trained without the loss functions that includes the Eikonal equation (second), traditional PINNs (third) and a graph convolutional network (last).

Figures 1 and 3 show the results of these experiments. For  $\Delta$ -PINNs and the graph convolutional network we select the best out of 5 random initializations (see Appendix B.1). In the bottom row of Figure 1, we see the exact solution to the geodesic problem, the physics-informed neural network learned solution, the graph convolutional network and the proposed method. On one hand, we see that PINNs fail to capture the fast variations in the Cartesian space and then to predict a nearly constant intermediate value. On the other hand, we see that  $\Delta$ -PINNs can represent the exact solution with high accuracy. The graph convolutional network performs better than PINNs but struggle to correctly learn the level-sets of the solution. This is reflected in Figure 3, where we show the correlation between the predicted and ground truth data for train and test points. We see that  $\Delta$ -PINN achieves a high correlation in both training and testing data, while PINNs fail to fit both. When the physics is removed from  $\Delta$ -PINNs, the method can only overfit the training data with a poor performance in the test data. The errors and training times are summarized in Table 1. The normalized mean squared errors on the combined train and test dataset correspond to  $3.68 \cdot 10^{-3}$  for  $\Delta$ -PINNs, 0.99 for  $\Delta$ -NNs ( $\Delta$ -PINNs without physics), 0.98 for PINNs, and  $2.95 \cdot 10^{-2}$  for the GCN. These results show more than 2 orders of magnitude improvement for the proposed method over the traditional formulation, at the expense of small pre-processing step of computing the eigenfunctions of the Laplace-Beltrami operator for that geometry (see Section 3.4). It is worth noting that generating the solution of the Eikonal equation with the exact geodesic algorithm does not lead to a zero  $MSE_{PDE}$  loss as defined in Eq. (9) due to the underlying numerical discretization. If we evaluate this term using all the points in the mesh we obtain a residual value of  $2.11 \cdot 10^{-2}$ . Hence, the proposed method works even in the presence of imperfect physics, when the model is not exactly satisfied.

### 3.2. Heat transfer in a heat sink

In this experiment, we simulate a heat sink with convection losses in 2 dimensions and steady state. This can be expressed as the following boundary value problem

$$\begin{cases} -\Delta u(\mathbf{x}) = 0, & \mathbf{x} \in \mathcal{B}, \\ u(\mathbf{x}) = 1, & \mathbf{x} \in \Gamma_D, \\ \nabla u(\mathbf{x}) \cdot \mathbf{n} = 0.1u(\mathbf{x}), & \mathbf{x} \in \Gamma_C, \\ \nabla u(\mathbf{x}) \cdot \mathbf{n} = 0, & \mathbf{x} \in \Gamma_N. \end{cases} \quad (10)$$

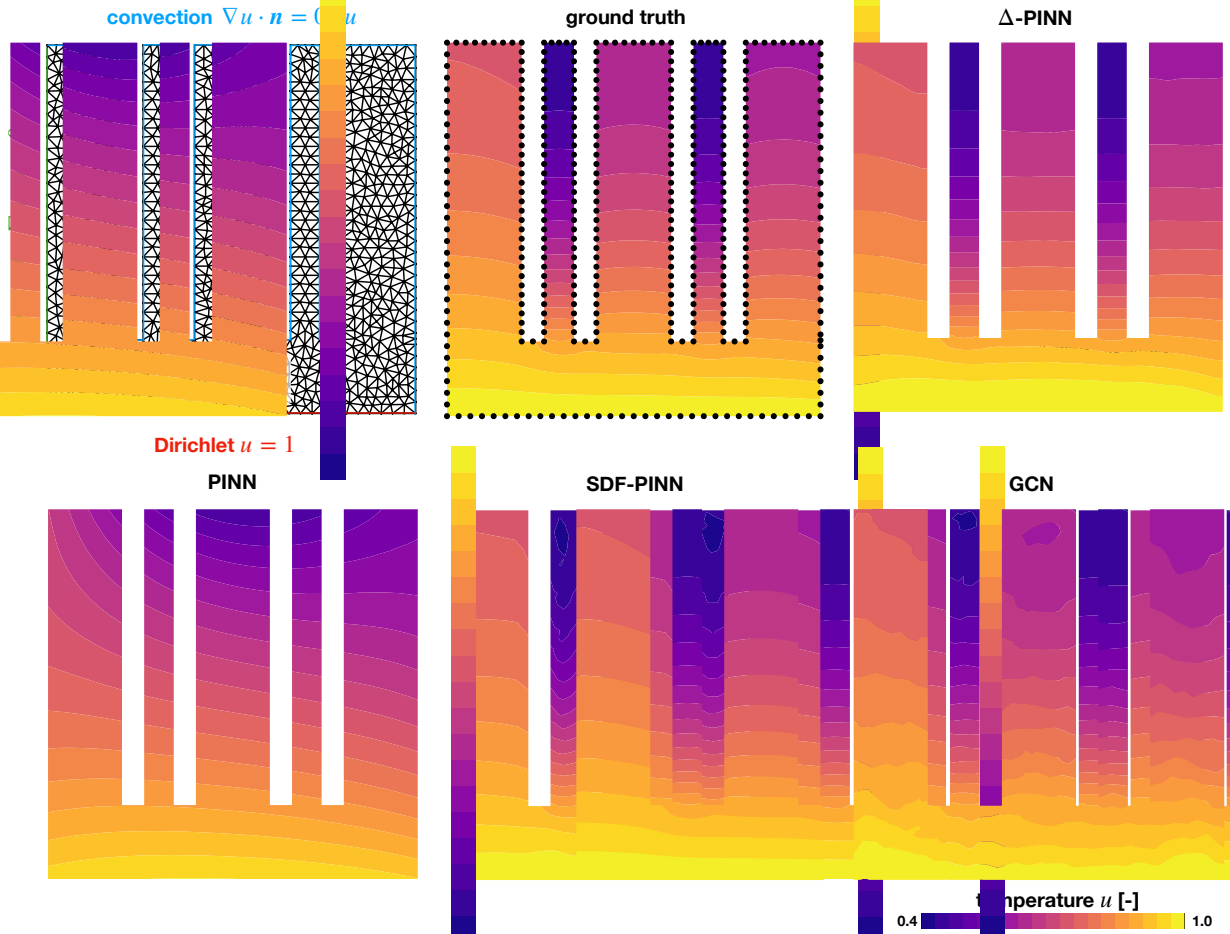


Figure 4: **Learning the temperature distribution of a heat sink from boundary measurements.** First, the boundary conditions and the finite element mesh used to create the solution. Second, the ground truth, and in the learned solution of (third)  $\Delta$ -PINNs, (forth) signed distance function PINNs and (last) traditional PINNs. The data points are shown on the ground truth panel in black.

We include three different types of boundary conditions: Dirichlet on  $\Gamma_D$ , Robin on  $\Gamma_C$ , and Neumann on  $\Gamma_N$ . The Dirichlet boundary condition is to represent another body with constant, higher than ambient, temperature, which the heat sink  $\mathcal{B}$  is attempting to dissipate. The Robin boundary condition represents a convective flux, which is proportional to the temperature  $u$ . The Neumann boundary condition is used to represent the symmetry of the domain. The geometry and location of the boundaries are shown in Figure 4. This example could be interpreted as a simplified model for the heat sink that is typically placed above a central processing unit (CPU) of a computer. To generate a ground truth solution for this problem we performed finite element simulations using the FEniCS library [29] on a

mesh with 1,289 nodes and 2,183 linear triangular elements. In this experiment we will attempt to solve the problem of learning the temperature inside the domain  $\mathcal{B}$  from the information of the temperature in the boundary  $\partial\mathcal{B}$ . We will again use the proposed  $\Delta$ -NNs, as well as conventional PINNs to solve this problem. In all cases, we will not inform the type of boundary conditions applied, and instead we only provide temperature measurements  $u_i$  at the boundary  $\partial\mathcal{B}$ . Thus, we will not consider the term  $MSE_b$  in the loss function defined in Eq. (1). In practice, this is important because the true form of the convective fluxes is often unknown or empirically approximated. For  $\Delta$ -PINNs we will approximate the Laplacian operator  $\Delta u$  with triangular finite elements using the definition of the operator  $\mathbf{A}$  shown in Eq. (5). Then, we can define the loss term

$$MSE_{PDE}(\boldsymbol{\theta}) = \sum_i^R \left( \sum_{j \in N(i)} A_{ij} \hat{u}_j \right)^2, \quad (11)$$

where the index  $i$  represents the nodes of the mesh inside the domain  $\mathcal{B}$ ,  $j \in N(i)$  represents the neighbor nodes of the node  $i$ , including itself. The term  $\hat{u}_j$  represents the output of the neural network at the nodal locations  $j$  that depends on trainable parameters  $\boldsymbol{\theta}$ . For traditional PINNs, we use automatic differentiation to compute  $\Delta \hat{u}$  and construct the loss term  $MSE_{PDE}$ . We also compare to physics-informed neural network that exactly imposes the boundary data using signed distance functions [48], which can only work in the case of a flat surface or 3D solid, detailed in Appendix B.3, and the physics-informed graph convolutional network, introduced the previous section, with matched number of parameters. We use 50 eigenfunctions to represent the domain  $\mathcal{B}$  for  $\Delta$ -PINNs, and 3 hidden layers of 100 neurons for all cases. We train the network with ADAM [24] for 50,000 iterations using a batch size of 30 samples to evaluate each of the terms of the loss function. We use 393 values of  $u$  located at the boundaries as training data, as shown in Figure 4. We note that we use the same operator, the Laplacian, for the PDE that governs this problem and to construct the input of the neural network. However, the eigenfunctions are computed with homogeneous Neumann boundary conditions, which guarantees that the eigenfunctions  $v_i$  are not solutions to the boundary value problem shown in Eq. (10) since they have different boundary conditions.

The results of this experiment are summarized in Figures 4, 5 and Table 1. First, we see that the geometry of the heat sink greatly influences the solution, as shown in Figure 4. The narrow fins have more temperature reduction than the wide ones. Qualitatively, we observe that  $\Delta$ -PINN produces the closest temperature distribution to the ground truth solution. The method is able to produce different temperature distributions for the different fins, which may be close in Euclidean distance, but are far apart in the intrinsic distance. The signed distance function PINNs produce a reasonable approximation everywhere except for the narrow fins, where there is an artificial curvature. Finally, traditional PINNs tend to favor satisfying the  $MSE_{PDE}$ , producing effectively a nearly linear solution for which trivially  $\Delta \hat{u} = 0$ . However, in this process the data provided at the boundaries is not fitted. Also, this method is not able to produce different temperature profiles for the different fins, correlating points that are close only in the cartesian space. Quantitatively, we see that the normalized mean squared error on the combined train and test sets drops 2 orders of magnitude for  $\Delta$ -PINNs when compared to traditional PINNs. The signed distance function PINN produces an error slightly lower than  $\Delta$ -PINNs, through the exact imposition of the data as boundary conditions. The graph convolutional network produces an slightly higher error, but with an irregular solution, as seen in Figure 4. Regarding the training times,  $\Delta$ -PINNs is the fastest of the methods that are informed by the geometry and produce accurate results. Also in Figure 5, we can see that for PINNs, the correlations reflect exactly the structure of the different fins. With this example, we have shown that a problem with simple physics, a linear problem, with some degree of complexity in the geometry of the domain may cause PINNs to fail while  $\Delta$ -PINN may successfully work.

### 3.3. Poisson equation with exact eigenfunctions

In this example, we select a case that should favor traditional PINNs: solving a Poisson equation in a simple square domain. Here, we fabricate the following solution

$$u(x, y) = (x^2 - 1)(y^2 - 1) \exp(-(x - y)^2/l^2) \quad (12)$$

which can be seen in the left panel of Figure 6. Then, we define the following boundary value problem to be tackled by PINNs.

$$\begin{cases} -\Delta u(\mathbf{x}) = f(\mathbf{x}), & \mathbf{x} = \{x, y\} \in \mathcal{B}, \\ u(\mathbf{x}) = 0, & \mathbf{x} \in \partial\mathcal{B}. \end{cases} \quad (13)$$

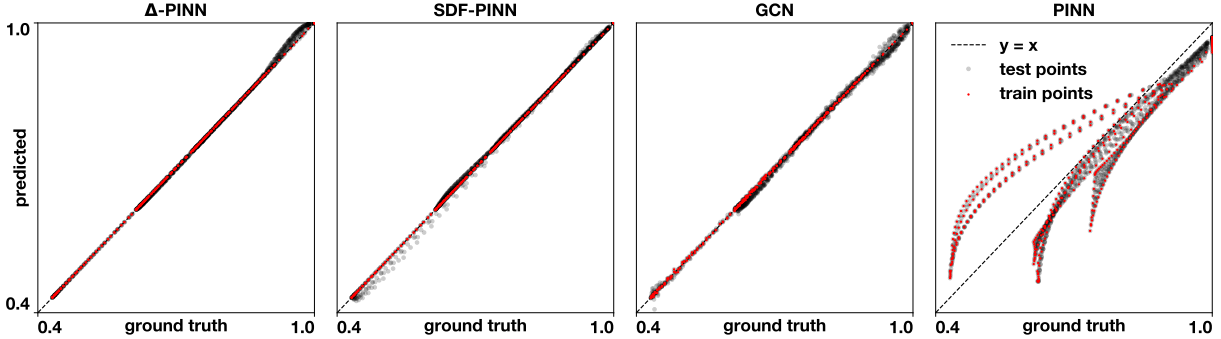


Figure 5: **Accuracy the heat sink example.** Correlation between predicted and ground truth values of temperature for  $\Delta$ -PINNs (left), signed distance function PINNs (center) and traditional PINNs (right).

The domain  $\mathcal{B}$  is defined by a square in  $[-1, 1] \times [-1, 1]$ . The expression for  $f(\mathbf{x})$  can be obtained by applying the Laplacian to the manufactured solution  $u(\mathbf{x})$ . In this domain, we can compute the eigenfunctions of the Laplace operator with homogeneous Neumann boundary conditions analytically, which correspond to

$$v_{l,m}(x, y) = \cos\left(\pi \frac{lx}{2}\right) \cos\left(\pi \frac{my}{2}\right), \quad (14)$$

with  $l, m = 1, \dots, \sqrt{N}$ , where  $N$  is the total number of eigenfunctions. We note that the boundary value problem described in Eq. (13) has Dirichlet boundary conditions, such that these eigenfunctions do not provide a suitable basis to solve this problem. In this case, we only provide data at the boundary  $\mathbf{x} \in \partial\mathcal{B}$  and the values of  $f(\mathbf{x})$  in the domain  $\mathbf{x} \in \mathcal{B}$ , effectively solving the forward boundary value problem (13). The partial differential equation loss in this example corresponds to

$$\text{MSE}_{\text{PDE}}(\boldsymbol{\theta}) = \sum_i^R \left( \sum_{j \in N(i)} (A_{ij} \hat{u}_j - M_{ij} f_j) \right)^2, \quad (15)$$

where the index  $i$  represents the nodes of the mesh inside the domain  $\mathcal{B}$ ,  $j \in N(i)$  represents the neighbor nodes of the node  $i$ , including itself. The term  $\hat{u}_j$  represents the output of the neural network at the nodal locations  $j$  that depends on trainable parameters  $\boldsymbol{\theta}$ , and  $f_i$  corresponds to  $f(\mathbf{x}_i)$ , with  $\mathbf{x}_i$  the position of node  $i$ . For traditional PINNs, we use automatic differentiation to compute  $\Delta \hat{u}$  and construct the loss term  $\text{MSE}_{\text{PDE}}$ . We use neural networks with 3 hidden layers of 100 neurons and train with ADAM for 50,000 iterations.

We perform a sensitivity study to understand the influence of the number of eigenfunctions and the size of the discretization used to evaluate the operator  $\Delta[\cdot]$  and the eigenfunctions computed numerically. We vary the number of eigenfunctions computed analytically and numerically from 9 to 400, and the size of finite elements between 0.02 to 0.2. Figures 6 and 7 summarize the results of this experiment. First, we note that traditional PINNs perform very well as expected, obtaining a mean squared error of  $1.72 \cdot 10^{-5}$ . Then, we observe that the results of  $\Delta$ -PINNs are sensitive to both the number of eigenfunctions and the discretization. When using the exact, analytical eigenfunctions, we are able to obtain low errors if we use more than 9 eigenfunctions for certain element sizes. When using the numerically obtained eigenfunctions, the same is true, except for the case of 400 eigenfunctions. In this case, we cannot use a bigger discretization than 0.1 because the number of nodes becomes less than 400. The discretization size has a bigger impact on the errors for both cases. There is a sweet spot between 0.066 and 0.1 where most cases produce low error. The minimum errors achieved in this range are  $1.94 \cdot 10^{-6}$  with the exact eigenfunctions and  $1.69 \cdot 10^{-6}$  with the numerical eigenfunctions. The error when the discretization is big is expected, since the Laplace operator will not be accurately approximated. The error when the discretization is small is not straightforward to explain, but we hypothesize that in these cases the  $\text{MSE}_{\text{PDE}}$  term becomes less important during training as the differences for  $\hat{u}$  become smaller as the scale of the element decreases. In Figure 6, we can see qualitatively that both PINNs and  $\Delta$ -PINNs can successfully solve this boundary value problem.

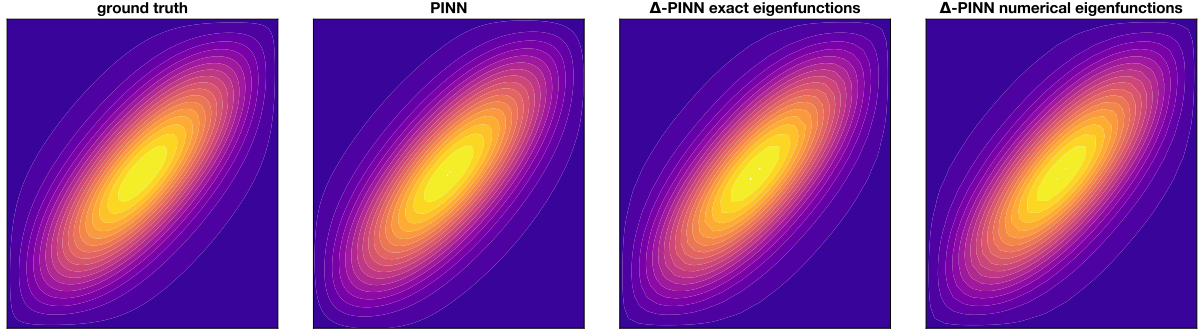


Figure 6: **Poisson example.** The ground truth manufactured solution, the approximation of traditional PINNs,  $\Delta$ -PINNs using the exact eigenfunctions as input and  $\Delta$ -PINNs using numerically approximated eigenfunctions by the finite element methods. For both cases of  $\Delta$ -PINNs, we use 100 eigenfunctions and an element size = 0.066 to discretize the operators.

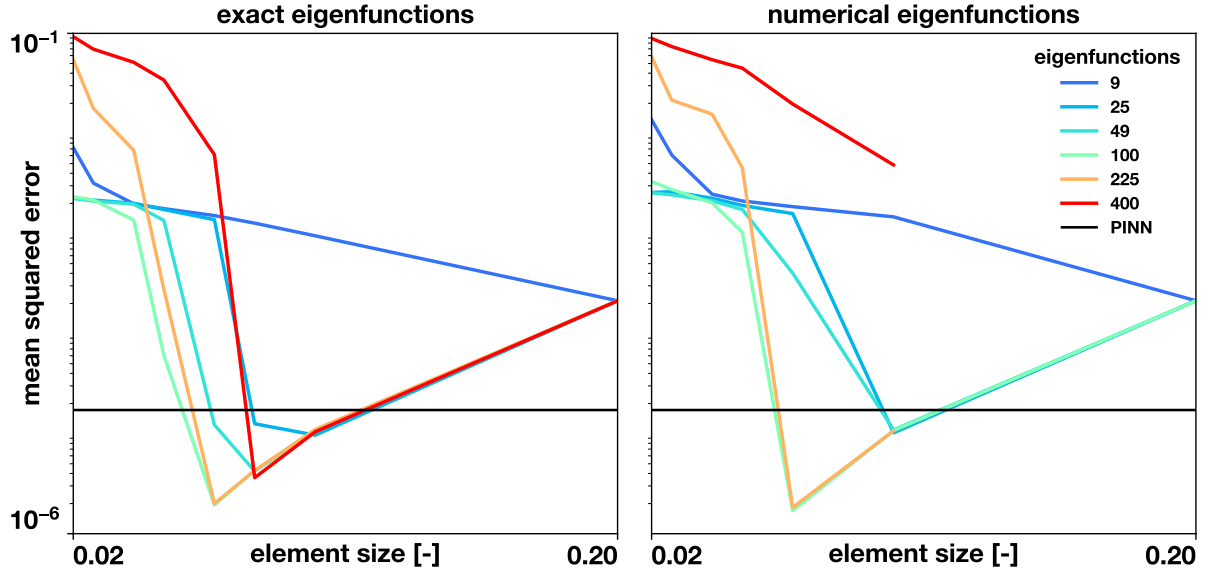


Figure 7: **Poisson example sensitivity analysis.** We run the Poisson example varying the two hyper parameters introduced by  $\Delta$ -PINNs: the number of eigenfunctions used as input and the element size used to discretize the operators. We test  $\Delta$ -PINNs using the exact eigenfunctions and the ones approximated by finite elements to understand the impact of this approximation.

### 3.4. $\Delta$ -PINNs on large meshes

In this section we show the time that it takes to compute the eigenfunctions of the Laplace-Beltrami operator of different sizes. We use the FEniCS library [29] to assemble the operators, and the SLEPc library [18] to solve the eigen-problem. We take 14 geometries from an open source repository<sup>1</sup> and compute 100 eigenfunctions. We use only 1 Intel(R) Xeon(R) CPUs (2.20GHz) for the calculations. The results are summarized in Figure 8. For the largest mesh with 134,345 nodes, the assembly of the operators and solving the eigen-problem took less than 35 seconds. This amount of nodes can be used to describe complex geometries. We also see excellent scaling with respect to the number of nodes. In this regard, training both traditional PINNs and  $\Delta$ -PINNs remains the largest computational burden in the process, and the computational cost of computing the eigenfunctions can be considered as a simple

<sup>1</sup><https://github.com/alecjacobson/common-3d-test-models>. Last accessed: 2023-06-16.

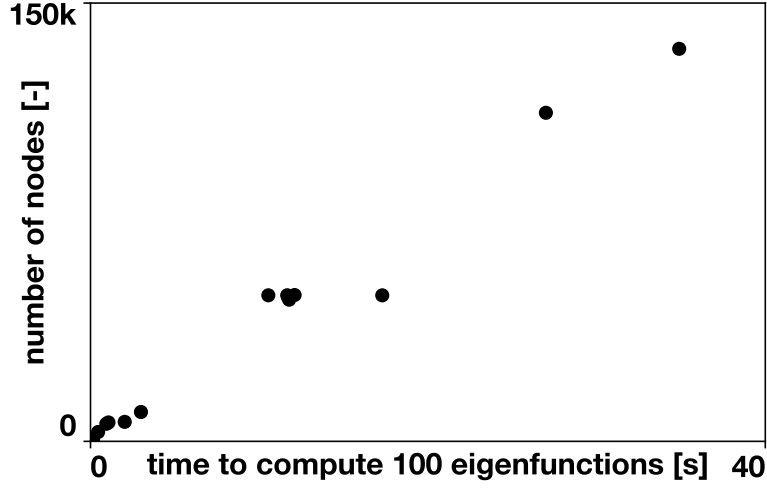


Figure 8: **Scaling of the eigenfunction computation.** We compute 100 eigenfunctions for a variety of meshes.

pre-processing step. We solve a partial differential equation on a large mesh with 99,970 triangles and 49,987 nodes from the model called Lucy. We set the following screened Poisson equation:

$$\begin{cases} -\Delta_S u + u = f, \\ f = (\sin(3\pi x) + \cos(3\pi y) + \sin(3\pi z))/3, \end{cases} \quad (16)$$

where  $\{x, y, z\}$  are the Cartesian coordinates of nodes. We note that this equation does not require boundary conditions to be solved in a closed surface. We generate the ground truth solution using finite elements, shown in Figure 9, left. The source term  $f$  is shown in Figure 9, right. We train  $\Delta$ -PINN using 100 eigenfunctions, 2 hidden layers of 100 neurons. We reformulate the partial differential equation in an energy form for the  $\text{MSE}_{\text{PDE}}$  term:

$$E(u) = \int_{\mathcal{B}} \left( \frac{1}{2} \|\nabla_S u\|^2 + \frac{1}{2} u^2 - uf \right) dx \quad (17)$$

Minimizing this energy is equivalent to solving the partial differential equation (16). This expression can be written in a discrete finite element form for the neural network nodal predictions  $\hat{u}$ :

$$\hat{E}(\hat{u}) = \sum_{r=1}^R \left( \frac{1}{2} (\mathbf{B}_r^e \hat{u}_r^e) \cdot (\mathbf{B}_r^e \hat{u}_r^e) + \frac{1}{6} A_r \hat{u}_r^e \cdot \hat{u}_r^e + \frac{1}{3} A_r \hat{u}_r^e \cdot \mathbf{f}_r^e \right) \quad (18)$$

where  $\hat{u}_r^e$  represents the output of the neural network at the nodes of triangle  $r$ ,  $A_r$  represents the area of the triangle  $r$ ,  $\mathbf{f}_r^e$  represents the source term evaluated at nodal positions of triangle  $r$ , and the matrix  $\mathbf{B}_r^e$  is the gradient operator for the triangle  $r$  introduced earlier and detailed in Appendix A. For simplicity, we use a lumped mass matrix, which assigns the same “mass” to all the nodes in the triangle, corresponding to  $A_r/3$ . As it would be too expensive to compute the energy in (18) for all iterations, we use only a mini-batch of triangles to estimate it. We note that this is a forward problem without boundary conditions, so the terms  $\text{MSE}_{\text{data}}$  and  $\text{MSE}_b$  are excluded from the loss function. We train for 2,000 iterations with batch size 1,000 with a learning rate of  $10^{-4}$ .

We obtain excellent agreement with the ground truth solution as shown in Figure 9, obtaining a mean squared error of  $9.25 \cdot 10^{-6}$ . Thus, we can see that  $\Delta$ -PINNs works well for large meshes, and that the eigenfunctions can be computed quickly.

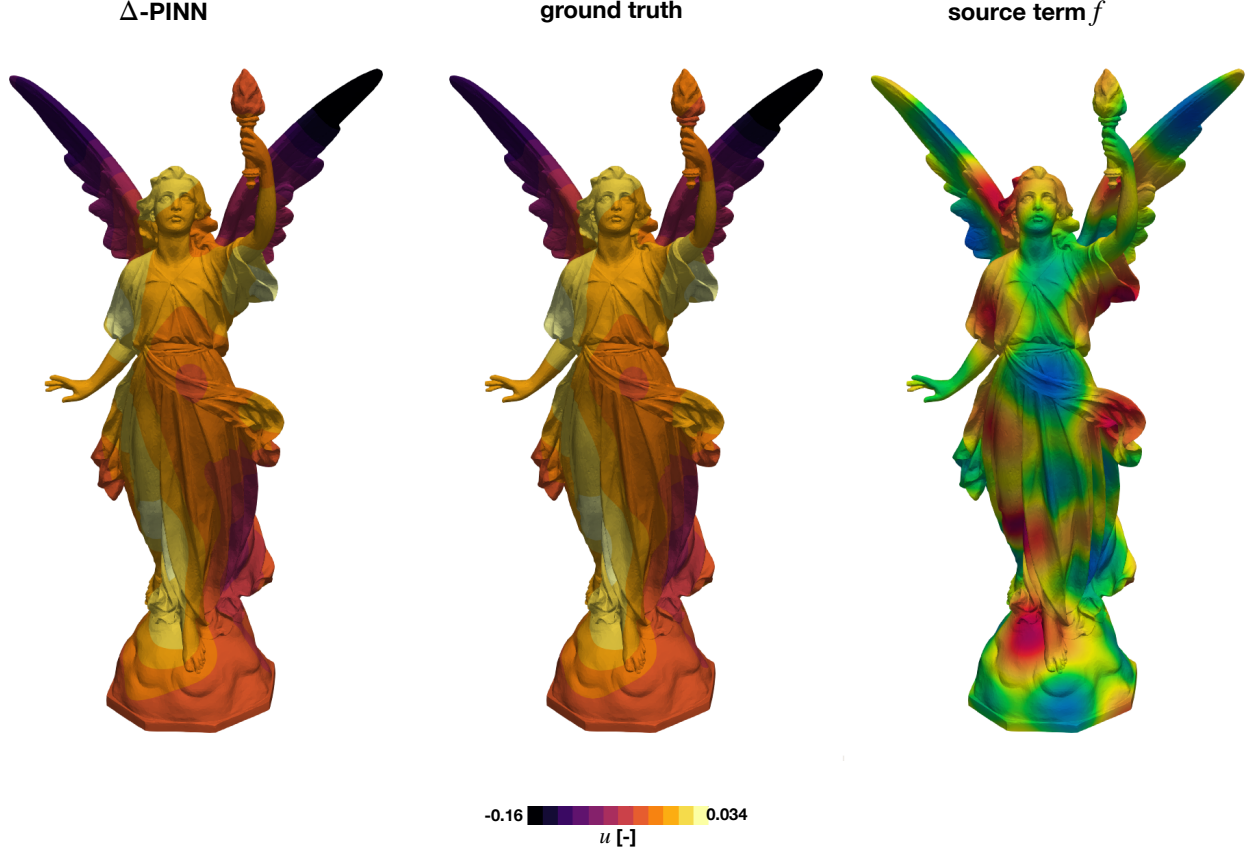


Figure 9: **Solving a partial differential equation on a large mesh.** We train  $\Delta$ -PINN on a mesh with 99,970 triangles and 49,987 nodes. On the left, is the approximation of  $\Delta$ -PINN of Eq. (16), center is the finite element solution, considered the ground truth, and right the source term form the screened Poisson Eq. (16).

### 3.5. Hyperelasticity

Next, we consider a hyperelasticity problem [19]. Let  $\mathbf{u} : \Omega_0 \rightarrow \mathbb{R}^2$  be the displacement field for a planar shape  $\Omega_0 \subset \mathbb{R}^2$ . The domain is  $\cap$ -shaped, formed by two semicircles of radius 1 and 0.2, respectively, and two arms of length 2, as shown in Figure 10. We seek for the displacement that minimizes the strain energy

$$E(\mathbf{u}) = \int_{\Omega_0} \mathcal{W}(\mathbf{F}) \, d\mathbf{x}, \quad \mathcal{W}(\mathbf{F}) = \mu(I_1 - 2 - 2 \ln J) + \lambda(J - 1)^2, \quad (19)$$

where  $\mathbf{F} = \mathbf{I} + \nabla \mathbf{u}$  is the deformation gradient,  $I_1(\mathbf{F}) := \text{tr}(\mathbf{F}^T \mathbf{F})$  is the first invariant, and  $J = \det \mathbf{F}$ . The positive numbers  $\mu$  and  $\lambda$  are material parameters, henceforth set to unity. The energy forms the  $\text{MSE}_{\text{PDE}}$  term. Using the same notation as in the previous section, we can approximate the energy as:

$$\hat{E}(\hat{\mathbf{u}}) = \sum_{r=1}^R A_r \mathcal{W}(\hat{\mathbf{F}}_r), \quad \hat{\mathbf{F}}_r = \mathbf{I} + \mathbf{B}^e \hat{\mathbf{u}}|_e \quad (20)$$

where  $A_r$  is the area of the triangle  $r$ ,  $\hat{\mathbf{F}}_r$  is the deformation gradient at the barycenter of the triangle  $r$ ,  $\mathbf{B}^e$  is the gradient operator defined in Appendix A, and  $\hat{\mathbf{u}}|_e$  are the displacements in the  $x$  and  $y$  directions in the nodes of the triangle predicted by the neural network. We also apply Dirichlet boundary conditions

$$\mathbf{u}|_{\Gamma_\ell} = [0, -\delta]^T, \quad \mathbf{u}|_{\Gamma_r} = [0, +\delta]^T, \quad (21)$$

where  $\delta = 0.4$  is a fixed parameter.

To approximate the solution with  $\Delta$ -PINN, we use 50 eigenfunctions. To avoid the potentially non diffeomorphic deformations that might be predicted by the random initialization of the network, we pre-train the network to output displacements close to zero for 40,000 iterations [30] with a learning rate of  $10^{-3}$ . The Dirichlet boundary conditions are informed through the  $\text{MSE}_{\text{data}}$  term, and which we multiply by  $10^3$  to closely inform them. Since the mesh is of small size, we train with the full batch, but the implementation is ready for mini-batch. We train for 100,000 iterations with the same learning rate used for pre-training.

As shown in Figure 10, we obtain an excellent agreement compared to the reference solution, with a mean square error of  $6.78 \cdot 10^{-6}$ . This example shows that we can use  $\Delta$ -PINNs to solve problems in non-linear mechanics.

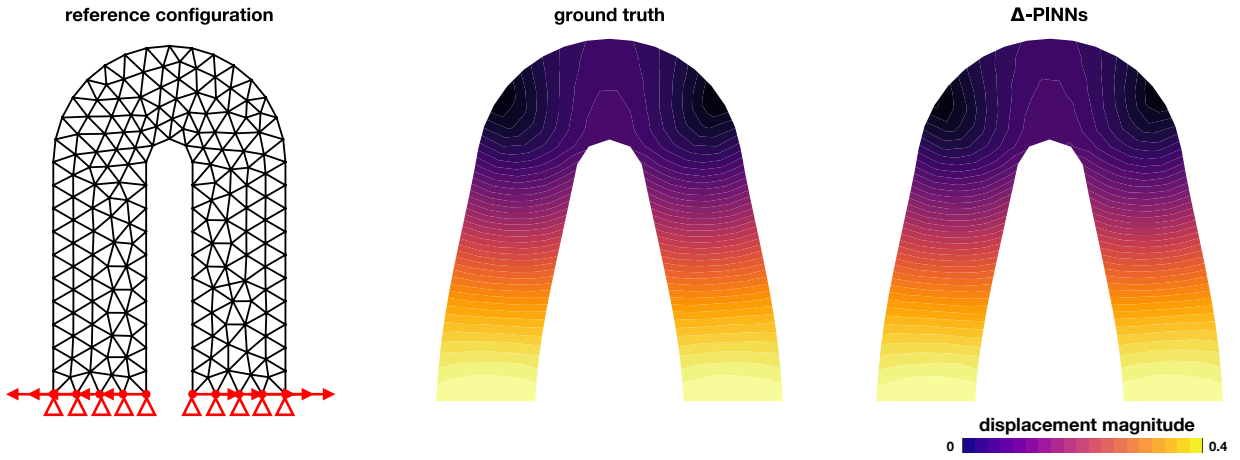


Figure 10: **Hyperelasticity**. Left panel, reference configuration, displaying the finite element mesh used to compute the ground truth solution, displayed in the middle panel. On the right panel, we show the  $\Delta$ -PINNs approximation.

### 3.6. Geodesic distance

In this Section we consider the problem of learning the geodesic distance function  $d(\mathbf{x}_1, \mathbf{x}_2)$  on a surface. The network architecture is structurally very similar to an unstacked deep operator network (DeepONets) [31, 53], albeit here we are not learning an operator. DeepONets are composed by a branch network that encodes the input functions and a trunk net that encodes the input position. The input function in our case corresponds to boundary condition of the Eikonal equation (8) and the input coordinate corresponds to points in the manifold. We note two properties of the geodesic distance function  $d(\cdot, \cdot)$ : first, it is symmetric,  $d(\mathbf{x}_1, \mathbf{x}_2) = d(\mathbf{x}_2, \mathbf{x}_1)$ , since the distance from  $\mathbf{x}_1$  to  $\mathbf{x}_2$  is the same as the distance from  $\mathbf{x}_2$  to  $\mathbf{x}_1$ . Second, the distance from a point to itself is zero, that is  $d(\mathbf{x}, \mathbf{x}) = 0$  for every point in the manifold. As in the other experiments, we represent points in the manifold by the eigenfunctions of the Laplace-Beltrami operator  $\mathbf{v}_i = [v_1(\mathbf{x}_i), v_2(\mathbf{x}_i), \dots, v_N(\mathbf{x}_i)]$ . With this in mind, we propose the following network architecture  $\hat{d}$  to approximate  $d$

$$\bar{d}(\mathbf{v}_1, \mathbf{v}_2) = \text{NN}(\mathbf{v}_1; \boldsymbol{\theta}_1) \cdot \text{NN}(\mathbf{v}_2; \boldsymbol{\theta}_2), \quad (22)$$

$$\hat{d}(\mathbf{v}_1, \mathbf{v}_2) = \frac{1}{2} \left( 1 - \frac{\mathbf{v}_1 \cdot \mathbf{v}_2}{\|\mathbf{v}_1\| \cdot \|\mathbf{v}_2\|} \right) (\bar{d}(\mathbf{v}_1, \mathbf{v}_2) + \bar{d}(\mathbf{v}_2, \mathbf{v}_1)), \quad (23)$$

where  $\boldsymbol{\theta}_1$  and  $\boldsymbol{\theta}_2$  represent the trainable parameters of the networks. This architecture automatically satisfies the symmetry and zero distance properties of the geodesic distance function. The network will be informed by the Eikonal equation, which should be satisfied at any point of the domain. In this case, we use the chain rule to compute the gradient  $\nabla_{\mathbf{x}_1} \hat{d} = \nabla_{\mathbf{v}_1} \hat{d} \cdot \nabla_{\mathbf{x}_1} \mathbf{v}$ , where the gradient is always the surface gradient. The gradient of the eigenfunctions with respect to the input positions  $\nabla_{\mathbf{x}_1} \mathbf{v}$  is computed with finite elements and gradient of the predicted distance function with respect to the input eigenfunctions  $\nabla_{\mathbf{v}_1} \hat{d}$  is computed with automatic differentiation. The loss function

to train the neural network still consists of the one detailed in Eq. (1), but in this case, we do not have boundary data and the partial differential equation loss takes the form:

$$\text{MSE}_{\text{PDE}}(\theta_1, \theta_2) = \frac{1}{R} \sum_i^R \left( \sqrt{(\nabla_{\mathbf{x}_1} \hat{d} \cdot \nabla_{\mathbf{x}_1} \hat{d})} - 1 \right)^2, \quad (24)$$

which is evaluated at the  $R$  triangle centroids of the mesh using a mini-batch strategy.

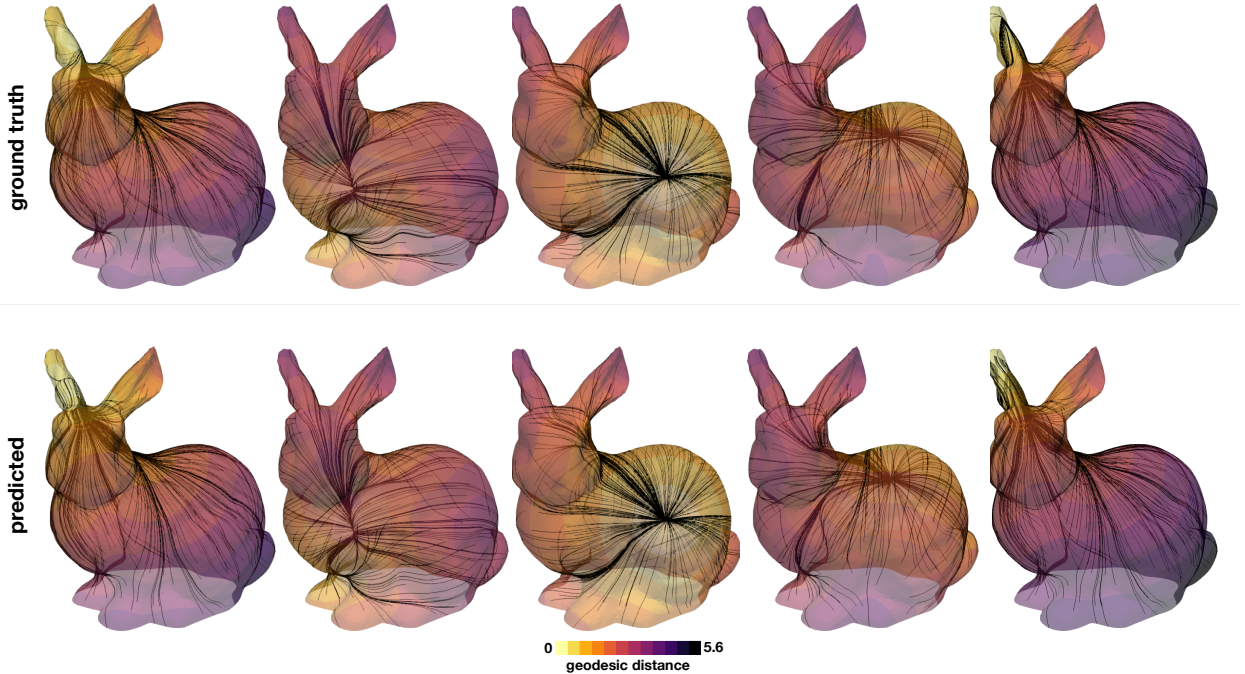


Figure 11: **Geodesics on a bunny.** We learn the geodesic distance between any two points in the bunny surface. We randomly select 5 points and show the ground truth and predicted geodesic distance between these points and the rest of the surface, and geodesic paths between 300 randomly selected points and these origin points.

We test the proposed methodology in the Stanford bunny [51], obtained from the software MeshMixer. This mesh has 5,550 vertices and 10,996 triangles, which results in 15,404,025 pairs of distance to be learned. We randomly select 50,000 pairs (0.32% of the total pairs) as training data, for which we compute the exact geodesic distance [34]. We use the 50 eigenfunctions associated with the lowest eigenvalues of the Laplace-Beltrami operator to define  $\mathbf{v}(\mathbf{x}_i)$ . Both for the trunk and branch network, we use 10 hidden layers of 200 neurons each. We train for 50,000 iterations with ADAM [24] with exponential decay of the learning rate.

To demonstrate the potential of this method, we also compute geodesic paths between  $\mathbf{x}_1$  and  $\mathbf{x}_2$  by solving the following initial value problem:

$$\begin{cases} \dot{\mathbf{x}}(t) = -\nabla_{\mathbf{x}(t)} d(\mathbf{x}(t), \mathbf{x}_2), \\ \mathbf{x}(0) = \mathbf{x}_1. \end{cases}$$

Some representative results of this method are shown in Figure 11, where we display the geodesic distance from 5 randomly selected points to the rest of the manifold for our method and the ground truth. We also show geodesic paths between 300 randomly selected points to each of the 5 origin points. We see qualitatively very good agreement in both the predicted geodesic distances and the geodesic paths. Furthermore, the geodesic paths are actually directed to the origin point, which shows that the learned geodesic distances continuously grow out of the origin point. Quantitatively, we evaluate the test error using 10,000 randomly selected pairs and obtained a mean absolute error normalized by the maximum geodesic distance of 0.57%.

## 4. Discussion

In this work, we present a novel method to use physics-informed neural networks in complex geometries by representing manifolds by the eigenfunctions of the Laplace-Beltrami operator. Given a mesh representing the geometry, we can compute these functions with standard finite elements. We show that this method outperforms the original formulation of PINNs, especially in cases where the points in the input domain are close in Euclidean distance but far in the intrinsic distance. We test our methodology by solving an inverse problem with the Eikonal equation, a Poisson, heat transfer and hyperelastic forward problem, and an operator learning problem for inferring the geodesic distance between two points on a complex manifold. We show better performance than a physics-informed graph convolutional network [16] and comparable performance to PINNs with signed distance functions, which is specially tailored for 2D problems with boundary data [48]. The Laplace-Beltrami eigenfunctions have been used in other applications of machine learning, such as point signatures in shapes [44, 49], shape descriptors [12], for neural fields [27], and to approximate kernels on manifolds for Gaussian process regression [4] and classification [14]. To our knowledge this is the first time they have been used in the context of physics-informed neural networks.

The proposed method can be seen as an extension of positional encoding methods [52], such as Fourier features [50], to arbitrary geometries. Furthermore, combining the Laplacian eigenfunctions in  $\mathbb{R}^N$ , we can recover a series of cosine functions when using Neumann boundary conditions and sine functions when using Dirichlet boundary conditions, which correspond to the encodings proposed in [52]. These techniques have significantly improved the performance of neural networks, including PINNs [54]. Nonetheless, we observed in our experiments that only using the eigenfunctions from the Laplacian with Neumann boundary conditions was enough to obtain accurate results. We see that including the physics of the problem greatly improves the results. Furthermore, we tested our method in a pure regression tasks in Appendix C and compared it to Gaussian process regression which can be naturally extended to work on manifolds. We see that neural networks with the eigenfunctions as input tend to overfit the data and the results depend heavily on the number of eigenfunctions used. This confirms the regularization effect of the physics, explaining the excellent performance in problems shown here. We also note that Gaussian process are an effective tool for regression on manifolds [4], but extending them to include physical knowledge expressed as non-linear constraints is cumbersome, as it requires approximate inference techniques and will inevitably suffer from the classical poor scaling of Gaussian processes [39].

In our experiment for the Poisson equation where we can directly compare to traditional PINNs (see Section 3.3), we observe that is possible to obtain similar levels of errors, showing that our method can also be used for simple domains. Furthermore, we did not see a decrease in performance when we compared the numerically obtained eigenfunctions versus the exact ones. The number of eigenfunctions used did alter the accuracy of our method. This quantity is a hyper-parameter that needs to be tuned, as for all common positional encodings [50, 52]. We also need to select a discretization size, which is a common hyperparameter with the graph convolutional network. The SDF-PINN lacks these hyperparameters, but it does not work on surfaces on 3D. The size of the discretization to compute the operators has an impact on the accuracy in a non-monotonic fashion. The way that changing the discretization affects the loss landscape and the training dynamics requires further study which are beyond the scope of this work.

Our current approach has some limitations. We numerically approximate the operators involved in the partial differential equations using finite elements. Although the gradient and the Laplacian, which are the most commonly used operators, can be approximated with linear elements, more sophisticated elements might be needed for other operators. And even though in this study we require a mesh to compute eigenfunctions and the operators, this approach is not conceptually limited to be mesh-free. We could compute the eigenfunctions using a point cloud Laplace-Beltrami operator [46] and we could approximate the gradient operator with traditional mesh-free methods [2]. We plan to pursue this avenue in the future. Finally, we also need to compute the eigenfunctions of the Laplace-Beltrami operator as a pre-processing step. Nonetheless, as we show in Section 3.4, this task takes just a few seconds even for complex meshes with more than  $10^5$  nodes, and as shown in Table 1, it is fraction of the training time.

As future work, we plan to expand this methodology to work on 3D solid geometries, for which we can compute the eigenfunctions of the Laplace operator. There are multiple opportunities in this area, as most partial differential equations are actually solved in this type of domains. We would also like to extend this approach to time dependent problems, where we can include time as an additional feature of the neural network. We envision that  $\Delta$ -PINNs will enlarge the possibilities for applications of physics-informed neural networks in more complex and realistic geometries.

## 5. Acknowledgments

This work was funded by ANID – Millennium Science Initiative Program – ICN2021\_004 and NCN19\_161 to FSC. FSC also acknowledges the support of the project FONDECYT-Iniciación 11220816. This work was financially supported by the Theo Rossi di Montelera Foundation, the Metis Foundation Sergio Mantegazza, the Fidinam Foundation, and the Horten Foundation to the Center for CCMC. SP also acknowledges the CSCS-Swiss National Supercomputing Centre (No. s1074), and the Swiss Heart Foundation (No. FF20042). This work was also supported by the European High-Performance Computing Joint Undertaking EuroHPC under grant agreement No. 955495 (MICROCARD) co-funded by the Horizon 2020 programme of the European Union (EU) and the Swiss State Secretariat for Education, Research and Innovation to SP. PP acknowledges support from the US Department of Energy under the Advanced Scientific Computing Research program (grant DE-SC0019116), the US Air Force Office of Scientific Research (grant AFOSR FA9550-20-1-0060)

## References

- [1] Babuška, I., Osborn, J., 1991. Eigenvalue problems, in: Ciarlet, P., Lions, J. (Eds.), *Handbook of Numerical Analysis*. Elsevier. volume 2. chapter 5, pp. 641–787.
- [2] Belytschko, T., Rabczuk, T., Huerta, A., Fernández-Méndez, S., 2004. *Meshfree Methods*. John Wiley & Sons, Ltd. chapter 10. pp. 279–306.
- [3] Berg, J., Nyström, K., 2018. A unified deep artificial neural network approach to partial differential equations in complex geometries. *Neurocomputing* 317, 28–41.
- [4] Borovitskiy, V., Terenin, A., Mostowsky, P., et al., 2020. Matérn Gaussian processes on Riemannian manifolds. *Advances in Neural Information Processing Systems* 33, 12426–12437.
- [5] Buffa, A., Sangalli, G., Vázquez, R., 2010. Isogeometric analysis in electromagnetics: B-splines approximation. *Computer Methods in Applied Mechanics and Engineering* 199, 1143–1152.
- [6] Cai, S., Wang, Z., Wang, S., Perdikaris, P., Karniadakis, G.E., 2021. Physics-informed neural networks for heat transfer problems. *Journal of Heat Transfer* 143.
- [7] Coifman, R.R., Lafon, S., 2006. Diffusion maps. *Applied and computational harmonic analysis* 21, 5–30.
- [8] Defferrard, M., Bresson, X., Vandergheynst, P., 2016. Convolutional neural networks on graphs with fast localized spectral filtering. *Advances in neural information processing systems* 29.
- [9] Do Carmo, M.P., 2016. *Differential geometry of curves and surfaces: revised and updated second edition*. Courier Dover Publications.
- [10] Dziuk, G., 1988. Finite Elements for the Beltrami operator on arbitrary surfaces, in: Hildebrandt, S., Leis, R. (Eds.), *Partial Differential Equations and Calculus of Variations*. Springer, pp. 142–155. doi:10.1007/BF0082865.
- [11] Evans, L.C., 2022. *Partial differential equations*. volume 19. American Mathematical Society.
- [12] Fang, Y., Xie, J., Dai, G., Wang, M., Zhu, F., Xu, T., Wong, E., 2015. 3d deep shape descriptor, in: *Proceedings of the IEEE Conference on Computer Vision and Pattern Recognition*, pp. 2319–2328.
- [13] Fang, Z., Zhang, J., Yang, X., 2021. A physics-informed neural network framework for partial differential equations on 3d surfaces: Time-dependent problems. *arXiv preprint arXiv:2103.13878* .
- [14] Gander, L., Pezzuto, S., Gharaviri, A., Krause, R., Perdikaris, P., Sahli Costabal, F., 2022. Fast characterization of inducible regions of atrial fibrillation models with multi-fidelity gaussian process classification. *Frontiers in Physiology* , 260.
- [15] Gao, H., Sun, L., Wang, J.X., 2021. Phygeonet: physics-informed geometry-adaptive convolutional neural networks for solving parameterized steady-state pdes on irregular domain. *Journal of Computational Physics* 428, 110079.
- [16] Gao, H., Zahr, M.J., Wang, J.X., 2022. Physics-informed graph neural galerkin networks: A unified framework for solving PDE-governed forward and inverse problems. *Computer Methods in Applied Mechanics and Engineering* 390, 114502.
- [17] Haghhighat, E., Raissi, M., Moure, A., Gomez, H., Juanes, R., 2021. A physics-informed deep learning framework for inversion and surrogate modeling in solid mechanics. *Computer Methods in Applied Mechanics and Engineering* 379, 113741.
- [18] Hernandez, V., Roman, J.E., Vidal, V., 2005. SLEPc: A scalable and flexible toolkit for the solution of eigenvalue problems. *ACM Trans. Math. Software* 31, 351–362.
- [19] Holzapfel, G., 2000. Nonlinear solid mechanics: A continuum approach for engineering. doi:10.1023/A:1020843529530.
- [20] Hughes, T.J., 2012. *The finite element method: linear static and dynamic finite element analysis*. Courier Corporation.
- [21] Jacobson, A., Panozzo, D., et al., 2018. libigl: A simple C++ geometry processing library. <https://libigl.github.io/>.
- [22] Jagtap, A.D., Karniadakis, G.E., 2020. Extended physics-informed neural networks (xpinn): A generalized space-time domain decomposition based deep learning framework for nonlinear partial differential equations. *Communications in Computational Physics* 28, 2002–2041.
- [23] Jagtap, A.D., Kawaguchi, K., Karniadakis, G.E., 2020. Adaptive activation functions accelerate convergence in deep and physics-informed neural networks. *Journal of Computational Physics* 404, 109136.
- [24] Kingma, D.P., Ba, J., 2014. Adam: A method for stochastic optimization. *arXiv preprint arXiv:1412.6980* .
- [25] Kipf, T.N., Welling, M., 2017. Semi-supervised classification with graph convolutional networks, in: *International Conference on Learning Representations*. URL: <https://openreview.net/forum?id=SU4ayYg1>.
- [26] Kissas, G., Yang, Y., Hwang, E., Witschey, W.R., Detre, J.A., Perdikaris, P., 2020. Machine learning in cardiovascular flows modeling: Predicting arterial blood pressure from non-invasive 4d flow mri data using physics-informed neural networks. *Computer Methods in Applied Mechanics and Engineering* 358, 112623.
- [27] Koestler, L., Grittner, D., Moeller, M., Cremers, D., Lähner, Z., 2022. Intrinsic neural fields: Learning functions on manifolds. *arXiv preprint arXiv:2203.07967* .

[28] Li, Z., Huang, D.Z., Liu, B., Anandkumar, A., 2022. Fourier neural operator with learned deformations for pdes on general geometries. arXiv preprint arXiv:2207.05209 .

[29] Logg, A., Mardal, K.A., Wells, G., 2012. Automated solution of differential equations by the finite element method: The FEniCS book. volume 84. Springer Science & Business Media.

[30] López, P.A., Mella, H., Uribe, S., Hurtado, D.E., Costabal, F.S., 2022. Warppinn: Cine-mr image registration with physics-informed neural networks. arXiv preprint arXiv:2211.12549 .

[31] Lu, L., Jin, P., Pang, G., Zhang, Z., Karniadakis, G.E., 2021. Learning nonlinear operators via DeepONet based on the universal approximation theorem of operators. *Nature machine intelligence* 3, 218–229.

[32] McFall, K.S., Mahan, J.R., 2009. Artificial neural network method for solution of boundary value problems with exact satisfaction of arbitrary boundary conditions. *IEEE Transactions on Neural Networks* 20, 1221–1233.

[33] Mildenhall, B., Srinivasan, P.P., Tancik, M., Barron, J.T., Ramamoorthi, R., Ng, R., 2020. Nerf: Representing scenes as neural radiance fields for view synthesis, in: European conference on computer vision, Springer. pp. 405–421.

[34] Mitchell, J.S., Mount, D.M., Papadimitriou, C.H., 1987. The discrete geodesic problem. *SIAM Journal on Computing* 16, 647–668.

[35] Mitzsch, S.K., Funke, S.W., Kuchta, M., 2021. Hybrid fem-nn models: Combining artificial neural networks with the finite element method. *Journal of Computational Physics* 446, 110651.

[36] Nabian, M.A., Gladstone, R.J., Meidani, H., 2021. Efficient training of physics-informed neural networks via importance sampling. *Computer-Aided Civil and Infrastructure Engineering* 36, 962–977.

[37] Pezzuto, S., Kalavský, P., Potse, M., Prinzen, F.W., Auricchio, A., Krause, R., 2017. Evaluation of a Rapid Anisotropic Model for ECG Simulation. *Frontiers in Physiology* 8, 265. doi:10.3389/fphys.2017.00265.

[38] Quarteroni, A., Valli, A., 2008. Numerical approximation of partial differential equations. volume 23. Springer Science & Business Media.

[39] Raissi, M., Perdikaris, P., Karniadakis, G.E., 2017. Machine learning of linear differential equations using gaussian processes. *Journal of Computational Physics* 348, 683–693.

[40] Raissi, M., Perdikaris, P., Karniadakis, G.E., 2019. Physics-informed neural networks: A deep learning framework for solving forward and inverse problems involving nonlinear partial differential equations. *Journal of Computational physics* 378, 686–707.

[41] Raissi, M., Yazdani, A., Karniadakis, G.E., 2020. Hidden fluid mechanics: Learning velocity and pressure fields from flow visualizations. *Science* 367, 1026–1030.

[42] Regazzoni, F., Pagani, S., Quarteroni, A., 2022. Universal solution manifold networks (USM-Nets): non-intrusive mesh-free surrogate models for problems in variable domains. *Journal of Biomechanical Engineering* 144, 121004.

[43] Ruiz Herrera, C., Grandits, T., Plank, G., Perdikaris, P., Sahli Costabal, F., Pezzuto, S., 2022. Physics-informed neural networks to learn cardiac fiber orientation from multiple electroanatomical maps. *Engineering with Computers* , 1–17.

[44] Rustamov, R.M., et al., 2007. Laplace-beltrami eigenfunctions for deformation invariant shape representation, in: Symposium on geometry processing, pp. 225–233.

[45] Sahli Costabal, F., Yang, Y., Perdikaris, P., Hurtado, D.E., Kuhl, E., 2020. Physics-informed neural networks for cardiac activation mapping. *Frontiers in Physics* 8, 42.

[46] Sharp, N., Crane, K., 2020. A laplacian for nonmanifold triangle meshes, in: Computer Graphics Forum, Wiley Online Library. pp. 69–80.

[47] Smith, J.D., Azizzadenesheli, K., Ross, Z.E., 2020. Eikonet: Solving the eikonal equation with deep neural networks. *IEEE Transactions on Geoscience and Remote Sensing* 59, 10685–10696.

[48] Sukumar, N., Srivastava, A., 2022. Exact imposition of boundary conditions with distance functions in physics-informed deep neural networks. *Computer Methods in Applied Mechanics and Engineering* 389, 114333.

[49] Sun, J., Ovsjanikov, M., Guibas, L., 2009. A concise and provably informative multi-scale signature based on heat diffusion, in: Computer graphics forum, Wiley Online Library. pp. 1383–1392.

[50] Tancik, M., Srinivasan, P., Mildenhall, B., Fridovich-Keil, S., Raghavan, N., Singhal, U., Ramamoorthi, R., Barron, J., Ng, R., 2020. Fourier features let networks learn high frequency functions in low dimensional domains. *Advances in Neural Information Processing Systems* 33, 7537–7547.

[51] Turk, G., Levoy, M., 1994. Zippered polygon meshes from range images, in: Proceedings of the 21st annual conference on Computer graphics and interactive techniques, pp. 311–318.

[52] Vaswani, A., Shazeer, N., Parmar, N., Uszkoreit, J., Jones, L., Gomez, A.N., Kaiser, Ł., Polosukhin, I., 2017. Attention is all you need. *Advances in neural information processing systems* 30.

[53] Wang, S., Wang, H., Perdikaris, P., 2021a. Learning the solution operator of parametric partial differential equations with physics-informed DeepONets. *Science advances* 7, eabi8605.

[54] Wang, S., Wang, H., Perdikaris, P., 2021b. On the eigenvector bias of fourier feature networks: From regression to solving multi-scale pdes with physics-informed neural networks. *Computer Methods in Applied Mechanics and Engineering* 384, 113938.

[55] Wang, S., Yu, X., Perdikaris, P., 2022. When and why PINNs fail to train: A neural tangent kernel perspective. *Journal of Computational Physics* 449, 110768.

[56] Wang, Y., Solomon, J., 2019. Intrinsic and extrinsic operators for shape analysis, in: *Handbook of Numerical Analysis*. Elsevier. volume 20, pp. 41–115.

## Appendix A. The use of finite elements in $\Delta$ -PINNs

In this section we provide a brief description of the finite element method in the context of the proposed methodology. In finite elements, we approximate the discretization of a function  $u(\mathbf{x})$  on a mesh with nodes and elements as

the sum of functions with compact support [20]

$$u(\mathbf{x}) = \sum_i^{n_{\text{nodes}}} N_i(\mathbf{x}) u_i, \quad (\text{A.1})$$

where  $N_i$  represent the so-called shape functions that are associated with node  $i$  of the mesh, and  $u_i$  is the value of the function at that node. In this work we only consider Lagrangian shape functions, that is those that satisfy the following delta property

$$N_i(\mathbf{x}_j) = \begin{cases} 1, & i = j, \\ 0, & i \neq j, \end{cases} \quad (\text{A.2})$$

where  $\mathbf{x}_j$  represents a nodal position. These functions also satisfy the partition of unity, such that  $\sum_i^{n_{\text{nodes}}} N_i(\mathbf{x}) = 1 \forall \mathbf{x}$ . An example of the shapes functions in 1D would be the hat (also called triangular) function defining a linear finite element. For a surface in 3D, the linear case corresponds to a piece-wise linear function that is 1 in node  $i$  and 0 in all neighboring nodes. In our case, we would like to compute the eigenfunctions of the Laplace-Beltrami operator using finite elements, which corresponds to solving the following boundary value problem

$$\begin{cases} -\Delta u(\mathbf{x}) = \lambda u(\mathbf{x}), & \mathbf{x} \in \mathcal{B}, \\ -\nabla u \cdot \mathbf{n} = 0, & \mathbf{x} \in \partial\mathcal{B}. \end{cases} \quad (\text{A.3})$$

We can rewrite this equation by multiplying by a test function  $w(\mathbf{x})$  and integrating in the entire domain

$$-\int_{\mathcal{B}} w(\Delta u(\mathbf{x}) + \lambda u(\mathbf{x})) \, d\mathbf{x} = 0. \quad (\text{A.4})$$

Using Green's first identity, we arrive at the variational formulation of the problem

$$\int_{\mathcal{B}} (\nabla w \cdot \nabla u - \lambda w u) \, d\mathbf{x} - \int_{\partial\mathcal{B}} w \nabla u \cdot \mathbf{n} \, d\sigma_{\mathbf{x}} = 0, \quad (\text{A.5})$$

for all possible choices of the test function  $w$  in some function space. The second term vanishes due to the boundary conditions of the problem. Typical choice for the space is the Sobolev space  $H^1(\mathcal{B})$  for Neumann boundary conditions and  $H_0^1(\mathcal{B})$  for Dirichlet conditions. The space  $H^1(\mathcal{B})$  contains the square-integrable functions (in the sense of Lebesgue) with square-integrable gradient.

The Galerkin approach for the numerical approximation of the eigenvalue problem consists in selecting a finite dimensional subspace of  $H^1(\Omega)$ . Here, we consider the classic finite element space of piecewise linear functions. Now, we approximate both functions with finite elements  $w(\mathbf{x}) \approx \sum_i^{n_{\text{nodes}}} N_i(\mathbf{x}) w_i$ ,  $u(\mathbf{x}) \approx \sum_j^{n_{\text{nodes}}} N_j(\mathbf{x}) u_j$ . Replacing, we obtain

$$\int_{\mathcal{B}} \sum_i^{n_{\text{nodes}}} \nabla N_i(\mathbf{x}) w_i \cdot \sum_j^{n_{\text{nodes}}} \nabla N_j(\mathbf{x}) u_j \, d\mathbf{x} - \lambda \int_{\mathcal{B}} \sum_i^{n_{\text{nodes}}} N_i(\mathbf{x}) w_i \sum_j^{n_{\text{nodes}}} N_j(\mathbf{x}) u_j \, d\mathbf{x} = 0, \quad (\text{A.6})$$

and since the nodal values  $u_j, w_i$  do not depend on  $\mathbf{x}$  we can rewrite

$$\sum_i^{n_{\text{nodes}}} w_i \sum_j^{n_{\text{nodes}}} u_j \left( \int_{\mathcal{B}} \nabla N_i(\mathbf{x}) \cdot \nabla N_j(\mathbf{x}) \, d\mathbf{x} - \lambda \int_{\mathcal{B}} N_i(\mathbf{x}) N_j(\mathbf{x}) \, d\mathbf{x} \right) = 0. \quad (\text{A.7})$$

Since this equation must hold for any test function, thus any values of  $w_i$ , we arrive at a system of equations

$$\sum_j^{n_{\text{nodes}}} u_j \left( \int_{\mathcal{B}} \nabla N_i(\mathbf{x}) \cdot \nabla N_j(\mathbf{x}) \, d\mathbf{x} - \lambda \int_{\mathcal{B}} N_i(\mathbf{x}) N_j(\mathbf{x}) \, d\mathbf{x} \right) = 0, \quad (\text{A.8})$$

for all  $i \leq n_{\text{nodes}}$ . This system can be written in matrix form by defining

$$\mathbf{A}_{ij} = \sum_{e=1}^{n_{\text{el}}} \int_{\mathcal{B}} \nabla N_j(\mathbf{x}) \cdot \nabla N_i(\mathbf{x}) \, d\mathbf{x}, \quad \mathbf{M}_{ij} = \sum_{e=1}^{n_{\text{el}}} \int_{\mathcal{B}} N_j(\mathbf{x}) N_i(\mathbf{x}) \, d\mathbf{x}, \quad (\text{A.9})$$

where  $\mathbf{A}$  represents the assembly of the local element matrices. Then, we solve the eigenvalue problem:

$$\mathbf{A}\mathbf{u} = \lambda \mathbf{M}\mathbf{u}, \quad (\text{A.10})$$

to obtain the eigenfunctions, where  $\mathbf{u} = [u_1, \dots, u_i, \dots, u_{n_{\text{nodes}}}]$ .

It is possible to show that the discrete set of eigenfunctions, obtained by solving the problem (A.10), converges to the analytical eigenfunctions as the mesh size goes to zero (under some uniformity assumptions in the way the limit is attained.) For linear basis functions and convex domains, the eigenvalues converge quadratically with respect to the mesh size [1]. The convergence of the eigenfunctions is linear in the energy norm and quadratic in the  $L^2$  norm. For non-convex domains, the convergence rate might be limited by the regularity of the eigenfunctions (e.g., the L-shaped domain.) Furthermore, the geometrical error in approximating the domain or the surface with a piece-wise linear complex may introduce additional approximation errors, usually in regions where the curvature is large. In this context, isoparametric or isogeometric finite elements are more indicated [5].

In this work, we use linear triangular elements, for which we will provide further detail. An important part of the proposed methodology is the computation of the gradient  $\nabla u$ . In linear finite elements, the gradient is constant inside the element. We compute the gradient in the element as  $(\nabla u)^e = \mathbf{B}^e \mathbf{u}^e$ , where

$$\mathbf{B}^e = \begin{bmatrix} N_{1,x} & N_{2,x} & N_{3,x} \\ N_{1,y} & N_{2,y} & N_{3,y} \end{bmatrix}, \quad (\text{A.11})$$

here  $N_{i,j}$  represents the derivative of shape function associated with node  $i$  of the element in the direction  $j$ . The vector  $\mathbf{u}^e = [u_1, u_2, u_3]$  is comprised of the  $u$  function values at the nodal locations of the triangle. Here we note that  $\{x, y\}$  is actually a local coordinate system of the triangle that will depend on its orientation. In general, the gradient with respect to the global coordinates  $\mathbf{X} = \{X, Y, Z\}$  can be obtained by changing the local to global coordinate systems with a rotation matrix  $\mathbf{R}^e$ :  $(\nabla_{\mathbf{X}} u)^e = \mathbf{R}^e \mathbf{B}^e \mathbf{u}^e$ . The rotation maps the normal direction of the triangle onto the  $Z$  direction. However, in all the applications of this manuscript this rotation matrix cancels, because we employ the surface gradient and the Laplace-Beltrami operator, see [10]. In the Eikonal equation, we can write the norm of the gradient as  $\sqrt{\mathbf{u}^{eT} \mathbf{B}^{eT} \mathbf{R}^{eT} \mathbf{R}^e \mathbf{B}^e \mathbf{u}^e}$ , but for any rotation matrix its inverse corresponds to its transpose, such that  $\mathbf{R}^{eT} \mathbf{R}^e = \mathbf{I}$ . The rotation matrix involved in the operation  $\nabla N_i \cdot \nabla N_j$  that defines the Laplacian also cancels following the same argument. We end this section by providing the specific form of the  $\mathbf{B}^e$  matrix for a triangular element. To make the description more concise we introduce the following notation:  $x_{ab} = x_a - x_b$  and  $y_{ab} = y_a - y_b$ , where  $x_i$  and  $y_i$  refer to the local coordinates of the node  $i$  in the triangle. We first introduce the area of the triangle  $A^e = (x_{13}y_{23} - x_{23}y_{13})/2$ . Then, we can define

$$\mathbf{B}^e = \frac{1}{2A^e} \begin{bmatrix} y_{23} & y_{31} & y_{12} \\ x_{32} & x_{13} & x_{21} \end{bmatrix}. \quad (\text{A.12})$$

## Appendix B. Comparison to other methods

Other than traditional PINNs, we compare to two other methods that are designed to work on complex geometries: a graph convolutional network [16] and a physics-informed neural network that exactly imposes boundary conditions with signed distance functions [48].

### Appendix B.1. Graph convolutional neural network

The authors of this approach [16] propose to use a graph convolutional network to approximate the solution of a partial differential equation. The input of this network will be locations of the nodes of the mesh. In general, convolution in a graph can be expressed as  $g_{\theta} \star \mathbf{x} = \mathbf{U} g_{\theta} \mathbf{U}^T$ , where  $g_{\theta}$  is a filter in Fourier domain and  $\mathbf{U}$  are the eigenvectors of the graph Laplacian [25]. This operator is different from Laplace-Beltrami operator, which we use here, in the

sense that it only encodes topological information about neighbouring nodes, but it completely lacks geometrical information. It is clear from the application of the graph convolution that it represents a linear combination of features. The result is then passed through a non-linear activation function and the convolution operation can be applied multiple times to create a deep graph-convolutional network. To avoid performing the eigen-decomposition of the graph Laplacian, it has been proposed to use Chebyshev polynomials [8]. The degree of the polynomial  $K$  represents the maximum separation of nodes that will be reached by the convolution. The authors set  $K = 10$ . Our approach is fundamentally different from the graph convolution, even though they are both related to the Laplacian. The graph convolution acts locally and propagates information to neighboring nodes [25]. Similarly, partial differential equations (PDEs) consider local differential operators, as certified by their sparsity when discretized with finite elements. However, the solution operator of such PDEs is global, and hence its finite dimensional counterpart is dense. Another way to see this is that local changes in the boundary conditions of the PDE yield global changes in the solution. For this reason, graph convolutional networks require either high order filters or multiple layers to propagate information across all nodes in the graph. In our approach, we encode global topological and geometric information about the domain in the Laplace-Beltrami eigenfunctions. These functions provide a suitable basis to approximate the solution of partial differential equations, which we non-linearly combine with a fully connected neural network.

In [16], the authors also compute the operators used in the underlying partial differential equations using the finite element method, which makes it a perfect candidate for comparison against our method. We compare both methods on the coil example with the Eikonal equation, which is detailed in Section 3.1. To approximately match the number of parameters used in  $\Delta$ -PINN, we use 3 hidden layers with 16 filters each, with ReLU activations for the Chebyshev convolutions with  $K = 10$ . We train both methods for the same number of iterations and we verified that both methods reached stable value of the loss. It is worth mentioning that training the graph convolutional network takes significantly longer than  $\Delta$ -PINNs because it does not allow for a mini-batch implementation: the output at one location potentially depends on every input node of the graph. In the coil example, with only 1,546 nodes,  $\Delta$ -PINNs is 9x faster to train than the graph convolutional network. This speed-up would only grow in more complex meshes, as the size of the mini-batch can be fixed for  $\Delta$ -PINNs and will grow for the graph convolutional network.

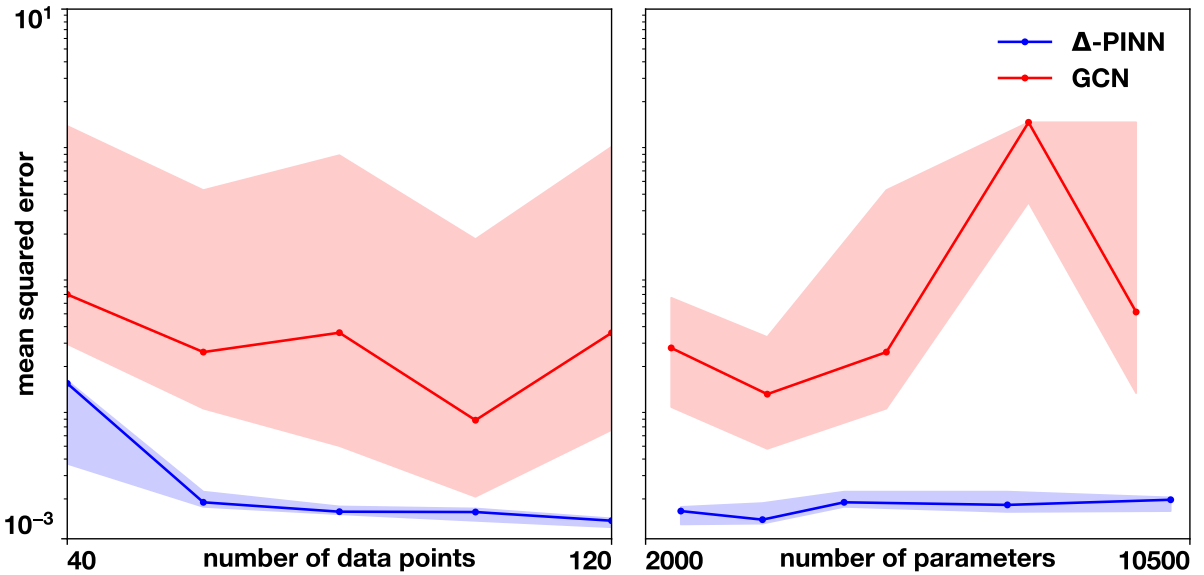


Figure B.12: **Ablation study comparing to graph convolutional networks.** We assess the test in the coil example varying the amount of data points provided with a fixed architecture (left) and vary the amount of parameters of each methodology when training with 60 data points. We repeat each run 5 times with different random initialization of the parameters and show the minimum and maximum error with filled band and the median with a solid line.

We finalize this comparison with an ablation study, by comparing the performance of the two methods in the coil

example. For all cases, we repeat the experiment with 5 different random initialization of the parameters. We compare the effect of adding more data points (Figure B.12, left) for fixed architectures used in Section 3.1. We see that for all cases,  $\Delta$ -PINNs outperforms the graph convolutional network, and we see a decrease in error as we add more data points. This behavior is lacking for the graph convolutional network, which increases the error when 120 data points are used. We also assess the effect of the number of parameters in both methods when training with 60 data points (Figure B.12, right). For  $\Delta$ -PINNs, we use only one hidden layer and 50 eigenfunctions, and vary the amount of neurons in the hidden layer. For the graph convolutional networks, we use 3 hidden layers and vary the size of these layers. In  $\Delta$ -PINNs, we see very little influence in the error if we change the number of parameters. For the graph convolutional network, we see that is very sensitive to the architecture choice in a non-trivial way. We also see than in general, the graph convolutional network is much more sensitive to changes in initialization than  $\Delta$ -PINNs.

#### Appendix B.2. Effect of the weight of partial differential equation loss in PINNs

In this study, when comparing different methodologies, we have kept the number of parameters, training settings, and loss formulations as close as possible to make comparisons. However, it is a well documented that the performance of PINNs is affected by the relative weight that the different loss term have [55]. For the coil example with the Eikonal equation, presented in Section 3.1, we study the effect of weighting the  $\text{MSE}_{\text{PDE}}$  term by a scalar  $w_r$ , while keeping the weight of  $\text{MSE}_{\text{data}}$  constant and set to 1. We vary  $w_r$  between  $10^{-8}$  and 1. The setup of the experiment are the same as detailed in Section 3.1. The results are shown in Figure B.13, where we observed that there is an optimal value of  $w_r$ , corresponding to  $10^{-2}$ . However, this value is still an order of magnitude higher than the error achieved by  $\Delta$ -PINNs. We note that neural network has the capacity to fit the provided data points, as the  $\text{MSE}_{\text{data}}$  reaches values below  $10^{-5}$  when  $w_r = 10^{-8}$ .

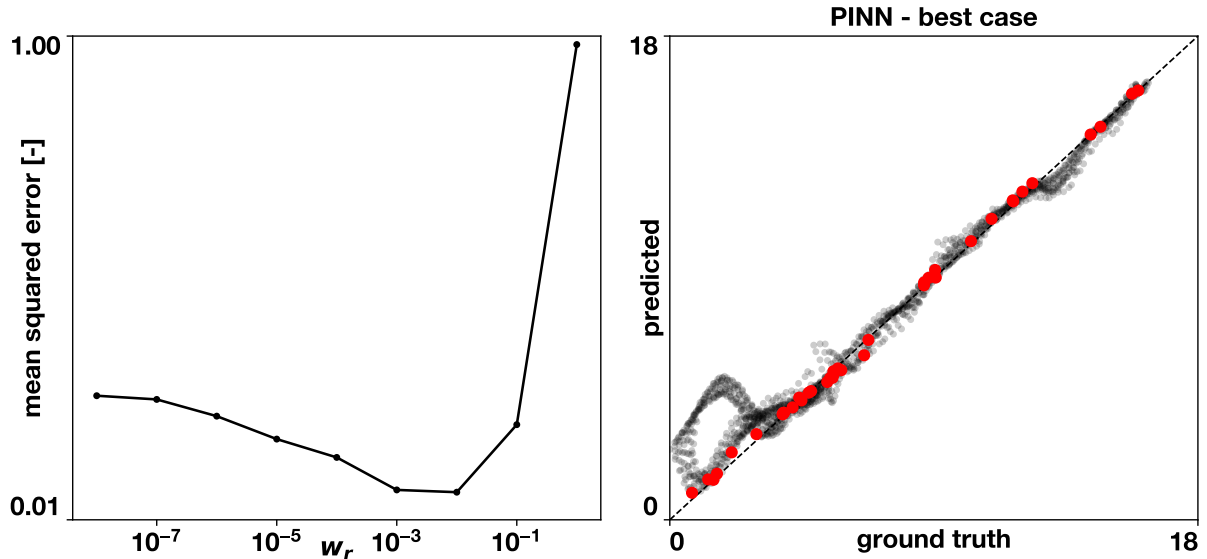


Figure B.13: Sensitivity with respect of the weight of the partial differential equation loss ( $w_r$ ) in PINNs. In the left we show the the mean squared error againts the solution of the Eikonal equation for different values of  $w_r$ . In the right panel we show the correlation between predicted and ground truth for the best case ( $w_r = 10^{-2}$ ).

#### Appendix B.3. Exact imposition of boundary conditions with signed distance functions

In [48], the authors focused on solving forward problems with PINNs. Typically, the boundary conditions are only approximately enforced through a term in the loss function, here shown in equation (1). To avoid this approach, which

may lead to errors as this loss term might not be completely minimized, the authors propose the following structure to approximate the solution of the partial differential equation

$$\hat{u}(\mathbf{x}, \boldsymbol{\theta}) = \text{NN}(\mathbf{x}, \boldsymbol{\theta})\phi(\mathbf{x}) + g(\mathbf{x}), \quad (\text{B.1})$$

where  $\text{NN}(\cdot, \boldsymbol{\theta})$  represents a fully connected neural network with trainable parameters  $\boldsymbol{\theta}$ ,  $\phi(\cdot)$  is signed distance function, which is zero at the boundary, and  $g(\cdot)$  is a function that interpolates the boundary conditions. With this construct,  $\hat{u}$  satisfies the boundary conditions for any parameters  $\boldsymbol{\theta}$ . The authors propose efficient ways to estimate the signed distance function  $\phi(\cdot)$  and they propose to use transfinite interpolation for  $g(\cdot)$ , which we implemented. We test this method in the heat sink example, detailed in Section 3.2. For this method, we treat the data at the boundary as boundary conditions, which are then interpolated. In order to match the amount of parameters of  $\Delta$ -PINNs, we use 3 hidden layers with 100 neurons each and we train for the same number of iterations. In Figures 4 and 5, we see that this approach improves significantly the performance of traditional PINNs, however it is not able to match the performance of  $\Delta$ -PINNs.

We also note that the scope of this method is much narrower than  $\Delta$ -PINNs. So far it has only been demonstrated to work on 2D examples and there is no direct path to make it work in surfaces in 3D, which is one of the strengths of  $\Delta$ -PINNs. The notion of the signed distance function is typically defined from the boundary of the domain, a curve in 2D or a surface in 3D. Since in this work we mainly focus on problems defined on surfaces in 3D there is no direct way to compute the signed distance function and apply this methodology. We also note that extending to SDF-PINNs as it is to 3D would be quite expensive computationally, as it is necessary to iterate over all the faces of the domain for a single prediction. Also, it does not allow for noise in the boundary conditions, because the interpolation  $g(\cdot)$  will exactly impose the noisy measurements.

## Appendix C. Regression with $\Delta$ -NN

In this section we test the capabilities of a neural network that takes as input the Laplace-Beltrami eigenfunctions to perform a regression task on a manifold. In this case, we do not include any physics that may act as a regularization of the predicted function. For this benchmark, we compare against Gaussian process regression with a Matérn kernel, which can be approximated on the manifold using the Laplace-Beltrami eigenfunctions as well [4]. We choose a dragon geometry with 9,057 vertices and 18,110 triangles. We create a synthetic ground truth function by computing the geodesic distance from a vertex  $d(\mathbf{x})$ :

$$f(\mathbf{x}) = \sin\left(\pi \frac{d(\mathbf{x})}{d_{\max}}\right), \quad (\text{C.1})$$

where  $d_{\max}$  corresponds to the maximum geodesic distance from the selected vertex. We train with 50, 100, 500 and 1000 data points, randomly selecting them. We repeat this process five times and report the median error. For the neural network ( $\Delta$ -NN), we train using 9, 25, 49, 100, 225 or 400 eigenfunctions. We use one hidden layer of 100 neurons and hyperbolic tangent activations. For the Gaussian process, we select  $\nu = 3/2$  for the Matérn kernel and approximate it with 1000 eigenfunctions. The results are shown in Figure C.14. In the lower right panel, we can see that the accuracy of  $\Delta$ -NN depends on the number of eigenfunctions used as input. When there are few data points available, it is preferable to have less eigenfunctions of lower frequencies to avoid overfitting. As the number of data points increases, more capacity is needed to approximate the data and the error decreases when more eigenfunctions are used. Nonetheless, using a high number of eigenfunctions, such as 225 and 400, never produces good results. On the other hand, Gaussian process regression excels in approximating this smooth function and always provides lower errors than  $\Delta$ -NNs. We also show in Figure C.14, top row, a comparison of the output produced by  $\Delta$ -NN and Gaussian process when training with 100 points. In general, where there is data, both methods do a good job approximating the function. However, in the absence of data points, such as the horns of the dragon,  $\Delta$ -NN tends to predict more extreme values that increase the overall error. In this case, the overall mean squared error drops from  $6.8 \cdot 10^{-2}$   $\Delta$ -NN to  $1.8 \cdot 10^{-2}$  for Gaussian process regression. We see that, in general,  $\Delta$ -NNs tend to overfit the data, and the addition of known physics across the domain has a regularization effect that improves the prediction, as seen in Figure 3 and 5.

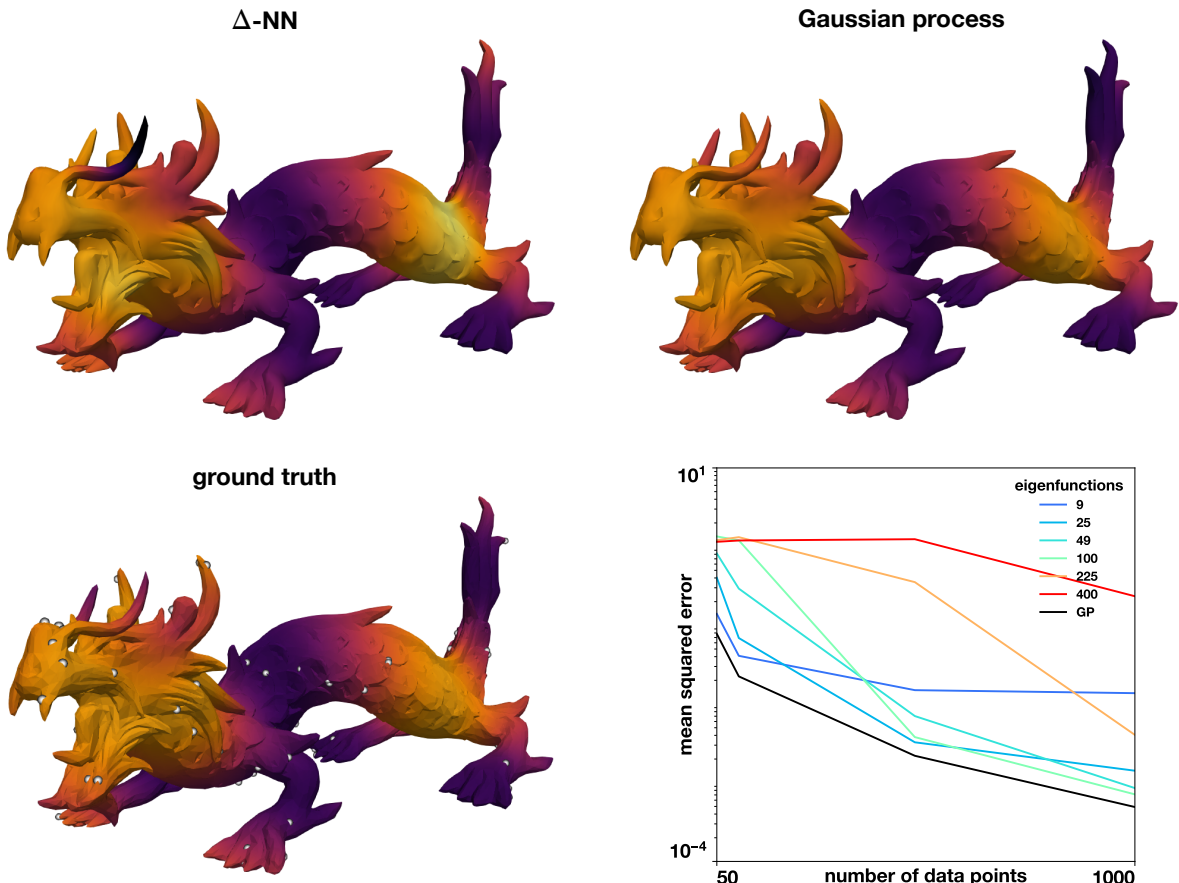


Figure C.14: **Regression on a dragon.** We show the results when 100 data points for  $\Delta$ -NN using 25 eigenfunctions and Gaussian process. The ground truth is shown in the lower left, along with the training points, shown in white. The error comparison for different levels of data availability and different number of eigenfunctions for  $\Delta$ -NN are shown in the lower right panel.